



Effect of metal-support interaction on activity and stability of Ni-CeO₂ catalyst for partial oxidation of methane

Rajib Kumar Singha, Astha Shukla, Aditya Yadav, L.N. Sivakumar Konathala, Rajaram Bal*

Nanocatalysis Area, Refining Technology Division, CSIR-Indian Institute of Petroleum, Dehradun 248005, Uttarakhand, India

ARTICLE INFO

Article history:

Received 17 June 2016

Received in revised form

23 September 2016

Accepted 26 September 2016

Available online 27 September 2016

Keywords:

Methane

Partial oxidation

Synthesis gas

Nickel

CeO₂ nanoparticles

ABSTRACT

The objective of the current study was to synthesize a nickel based catalyst with high activity at low temperature for partial oxidation of methane (POM). Ni-nanoparticles supported on CeO₂ nanoparticles were synthesized by two step preparation method. First, 30–50 nm CeO₂ was synthesized by solvo-thermal method and then Ni- nanoparticles were deposited over it following a newly developed procedure, where cetyltrimethylammonium bromide (CTAB) acted as morphology controlling agent and polyvinylpyrrolidone (PVP) as size controlling agent for nickel nanoparticles. The characterizations of synthesized catalysts were done by BET-Surface area, XRD, SEM, TEM, TPR, H₂-chemisorption, TGA and XPS analysis. The catalysts showed excellent coke resisting ability during POM and produces synthesis gas with H₂/CO ratio almost 2. The catalyst activated methane at 400 °C with 10% methane conversion and converts methane almost completely at 800 °C. The catalyst showed above 98% methane conversion at 800 °C during 90 h of time on stream (TOS) reaction with H₂/CO ratio 1.98. Average 5.5 nm Ni particles, use of CeO₂ as a support played a very crucial role for methane activation at such lower temperature. The synergistic effect between small Ni-nanoparticles and CeO₂ nanoparticles of Ni-CeO₂ catalyst is the main reason for such activity. Detailed study of other reaction parameters like temperature, Ni loading, weight hourly space velocity (WHSV) was also carried out and reported.

© 2016 Elsevier B.V. All rights reserved.

1. Introduction

Methane, the predominant component of natural gas, is considered to be a major energy source for the future [1–3]. Methane is a major greenhouse gas with much higher greenhouse potential than CO₂ [4]. It is gas in normal atmospheric condition and its storage and transportation problems prompted researchers to find out an alternative to utilize this huge energy source. Methane can be converted directly into HCHO, CH₃OH, C₂H₄ etc. but low conversion and low selectivity to these products are the main problems as the products are more reactive than methane itself [5,6]. Nowadays, methane is industrially used to produce synthesis gas (a mixture of CO and hydrogen), the basic raw material for many industrial processes to produce other chemicals and synthetic fuels [6]. Steam reforming of methane (SRM) is the major large scale synthesis gas production process, which produces H₂/CO ratio 3 [7]. Again, the major problem with CO₂ reforming of methane is reverse water gas shift (RWGS) reaction and coking on catalyst surface [4,8], which reduces hydrogen selectivity and deactivates catalyst. POM effi-

ciently produces synthesis gas with H₂/CO ratio 2 and it is the exact requirement for methanol synthesis [9]. Presence of oxygen in the reaction feed of POM reduces carbon deposition problem by removing the coke as CO and/or CO₂ [10,11]. Now, as POM provides so many advantages, it has its own problems too. First of all, it is an exothermic reaction, and the hot spot generation during the process raises some safety issues. Another issue is the requirement of pure oxygen, which is a problem from economic point of view. Because of potential of the production of synthesis gas via POM, researchers are trying to establish this process with the help of a suitable catalyst.

Decades of extensive research revealed that noble metal like Pt, Ru, Rh, Ir [1,5,12] and transition metals like Ni, Fe, Co [1,13–16] are very reactive for the POM process. Noble metals have very high activity and much more coke resistive during POM but the abundance and high cost limited its commercial application. From the reactivity point of view, Ni is the only transition metal with comparable activity to the noble metals. Low cost and high abundance of Ni makes it Holy Grail for methane activation. The problem with Ni catalysts is its coke sensitivity. Carbon accumulation on Ni surfaces during catalysis deactivates the catalysts rapidly and also causes reactor plugging [2]. Nano regime supported Ni catalysts are reported to be very much coke resistive [8] and efficiently pro-

* Corresponding author.

E-mail addresses: raja@iip.res.in, rajab.73@yahoo.com (R. Bal).



duce synthesis gas with H₂/CO ratio 2 during POM. Type of support is very crucial for obtaining resistance towards coking. Numerous reports showed applications with oxide supports like SiO₂, Al₂O₃, MgO, ZrO₂, CeO₂ etc [1,3,5,17]. CeO₂ is a suitable support for POM with high thermal stability, coke resisting behavior and very good redox properties [1,3,5,18,19]. CeO₂ is very well known for its oxygen storage property [20] and decreases coke formation by modifying the structural and electronic properties of catalysts [3,5]. Surface oxygen from cerium oxide reacts with carbonaceous species deposited on catalyst surface and again it gets re-oxidized by the gaseous oxidants in reaction system [10,11].

Metal-support interaction plays very significant role in controlling particle size, oxygen availability and coke resistance property of the catalyst. Strong metal-support interaction helps in formation of small and highly dispersed particles, resists sintering of catalysts particles during catalysis [4,21,22] and improves oxygen availability of the catalyst. The oxygen species at the metal-support interface are easily reducible [23,24] and during catalysis the oxygen species near the active metal removes the deposited carbon from catalyst surface improving the coke resistant property of catalyst [23–25]. Now, mechanism of POM reaction is highly dependent on catalyst properties. Eiras et al. [26] reported that POM reaction via direct route is theoretically possible. Recently we have reported Pt-CeO₂ catalyst for POM reaction at 350 °C [5]. At this much lower temperature CO₂ reforming or steam reforming of methane is not possible as much higher temperature is needed for these two reactions [21]. So, the formation of syngas at this temperature (350 °C) can only take place via direct route only. Choudhary et al. [1] reported that at very short contact time, if the POM reaction proceeds through indirect mechanism, there should be only combustion product present in the product gas, no POM product should be present because CO₂ reforming and Steam reforming of methane follows very slow kinetics.

Ni-MgO catalyst was reported by Kirillov et al. for POM with 75% of methane conversion with drastic decrease in conversion to 55% only after 24 h of time on stream (TOS) at 800 °C [27]. Asencios et al. reported NiO-MgO-ZrO₂ catalyst for POM with ≥90% of methane conversion at 750 °C but catalyst was deactivated by coking [10]. Green and his group [6] also reported costly molybdenum carbide catalyst for POM at very low gas hourly space velocity (GHSV) (2000 h⁻¹) and high pressure with 96% methane conversion at 900 °C. 96% methane conversion at 800 °C was reported by Li et al. over lanthanum doped Ni-SiO₂ core shell catalyst for POM with 65 h of time on stream stability at 700 °C [28]. Ni/CeZrO₂ catalyst with 7 h of TOS stability at 700 °C was reported by Larimi et al. with methane conversion above 80% [29]. Özdemir et al. [30] reported 89% methane conversion at 800 °C using air as oxidant over Ni/MgAl₂O₄ catalyst. Recently, Venezia and her group reported Ni-CeLa oxides [31] and Ni-CeO₂ catalysts prepared by different methods [32] for POM with above 90% of methane conversion at 800 °C. Oliveira et al. [33] recently reported 1.5% Rh-CeO₂ catalyst for POM. They reported 83.4% methane conversion at 800 °C.

Synthesis of a suitable catalyst with suitable support, which is thermally stable, coke resistant and exhibits excellent redox properties are the major challenge for methane activation purpose. Here, we are reporting synthesis of highly active and coke resistant Ni nanoparticles supported CeO₂ catalyst for the production of synthesis gas by POM.

2. Experimental

2.1. Catalyst preparation

Ni nanoparticle supported CeO₂ catalyst was synthesized by following two step preparation methods. First, 30–50 nm CeO₂

nano-particles was synthesized by a surfactant free solvo-thermal method, then Ni nanoparticles was deposited on nano-crystalline CeO₂. In a typical synthesis procedure, 4.3 g cerium nitrate hexahydrate [Ce(NO₃)₂·6H₂O] was dissolved in 125 ml ethanol by continuous stirring. After 2 h of stirring, 2% NH₃ solution was added very slowly to maintain pH at 7. Then after 1 h stirring of the whole mixture solution, it was autoclaved at 180 °C for 24 h. The autoclave was then cooled at 35 °C and a dry solid precipitate was obtained by evaporating the solvent by gradually increasing the temperature to 80 °C. The dried solid was then calcined at 700 °C for 6 h in air. The prepared cerium oxide was denoted as CeO₂^{*}.

In the second step, Ni nanoparticles were deposited on CeO₂^{*} by the following method. 10 ml ethanol was added with 0.4 g cetyltrimethylammonium bromide (CTAB) and 0.05 g polyvinylpyrrolidone (PVP) and dissolved the material. Then 0.25 g of nickel nitrate hexahydrate [Ni(NO₃)₂·6H₂O] dissolved in 20 ml H₂O was added slowly to the CTAB and PVP solution. The nickel salt solution was then added drop wise to 1 g of CeO₂^{*} dispersed in 100 ml ethanol and continued stirring for 2 h. Then 200 µl of hydrazine hydrate [NH₂NH₂·H₂O] was added with whole mixture solution to maintain the pH of the solution to 8 and continued stirring for 1 h. After 1 h of stirring the mixture solution was evaporated to dryness by gradual increase in temperature to 100 °C. The dried material was then finally calcined at 600 °C for 6 h in air and it was denoted as 5Ni-CeO₂^{*}. 2.5 Ni-CeO₂^{*} and 10Ni-CeO₂^{*} catalysts were also prepared for comparison. Here in the depicted method, CTAB controls Ni species morphology, PVP controls the size of Ni species and hydrazine acted as a reducing agent, capping agent and a base also. For comparison purpose Ni was also deposited by the here described method over commercial cerium oxide and it was denoted as 5Ni-CeO₂^{Com} (Supporting information).

Ni impregnated CeO₂ catalyst was synthesized using cerium oxide (CeO₂^{*}) for comparison (Supporting information). All the catalysts are designated as xNi-CeO₂, where 'x' is the wt% of Ni present in the catalyst.

2.2. Catalyst characterization

Characterizations of the synthesized catalysts were performed by BET-Surface area, XRD, SEM, TEM, H₂-Chemisorption, XPS and TGA/DTC. The detailed process is given in Supporting information.

2.3. Catalytic procedure

Catalysts activity tests were performed in a fixed-bed down flow reactor. Before the reaction, the catalysts were reduced with 20%H₂ balance He gas for 2 h at 600 °C. Due to exothermic nature of the reaction, catalyst was diluted with inert γ-Al₂O₃ and inert material (ground quartz) was used to dilute catalyst bed [34] and the reaction was performed at 350–800 °C, atmospheric pressure. The catalyst to diluent ratio 100:500 showed almost no temperature difference between the catalyst zones in the reactor. Typically, in a 6 mm quartz reactor, 60 mg of catalyst diluted with inert material was placed at the centre of two quartz wool plugs. WHSV was varied between 5000 and 200,000 ml g⁻¹ h⁻¹ with feed ratio of O₂:CH₄:He = 1:2:8.5 (mole ratio). The experimental set up to measure reaction temperature is discussed in detail in the Supporting information (Fig. S1). Analysis of the products were performed by online gas chromatography (Agilent 7890A) fitted with a TCD detector. Molecular sieves column was used for analyzing H₂ and PoraPack-Q column for analyzing CH₄, CO₂ and CO.

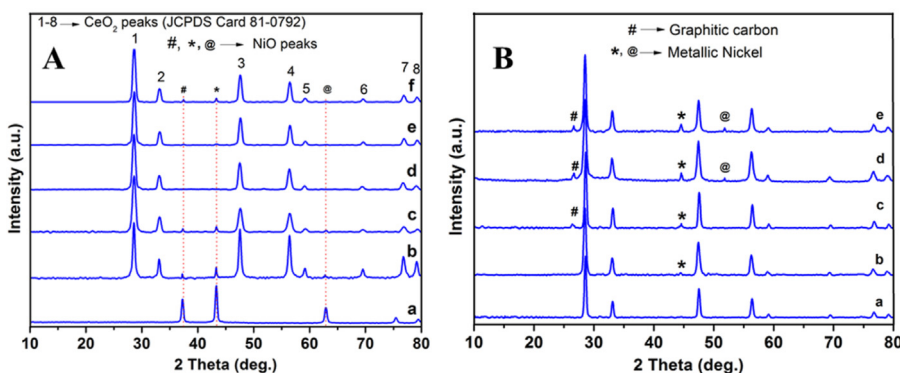


Fig. 1. (A) XRD patterns fresh (a) NiO, (b) 5Ni-CeO₂^{Com}, (c) 5Ni-CeO₂^{Imp}, (d) 2.5Ni-CeO₂^{*}, (e) 5Ni-CeO₂^{*} and (f) 10Ni-CeO₂^{*} catalyst. (B) XRD patterns spent (a) 2.5Ni-CeO₂^{*}, (b) 5Ni-CeO₂^{*}, (c) 10Ni-CeO₂^{*}, (d) 5Ni-CeO₂^{Com} and (e) 5Ni-CeO₂^{Imp} catalysts. Spent catalyst condition: Reaction time (20 h, TOS), Temperature (800 °C), Pressure (1 atm), WHSV (80,000 mg l⁻¹ h⁻¹), Feed ratio (O₂:CH₄:He = 1:2:8.5).

3. Results

3.1. Characterization

3.1.1. Physicochemical properties of the catalysts

The catalysts were characterized by BET-surface area (Table 1), metal dispersion (Table 1), XRD (Fig. 1), TPR (Fig. 2, Table 2), SEM (Fig. 3), TEM (Figs. 4–6), XPS (Fig. 7) and TGA/DTG (Fig. 8, Table 3). BET-Surface area measurement of prepared materials showed gradual increase in surface area with increasing nickel loading (Table 1). The surface area of 5Ni-CeO₂^{*} catalyst was 75.8 m²/g, whereas 5Ni-CeO₂^{Imp} catalyst showed surface area 16.5 m²/g. So, the catalyst synthesized by here described method showed surface area almost 5 times higher than the catalyst synthesized by conventional impregnation method. Therefore, the catalyst synthesis method played a very crucial role for physical properties of the catalyst [4,5,24]. Nickel species dispersion was also estimated by H₂-chemisorption experiment. The results showed that with increasing nickel loading, nickel species dispersion decreased gradually (Table 1). The reason may be agglomeration of nickel species with increase in nickel loading [4,5,24]. The catalyst synthesized by conventional impregnation method showed very low surface area with low dispersion of nickel species (Table 1). The reason may be the absence of any size controlling agent in impreg-

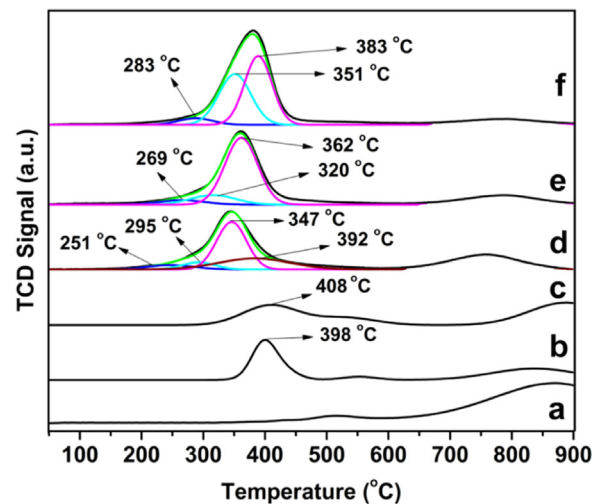


Fig. 2. H₂-TPR pattern of (a) CeO₂^{*}, (b) 5Ni-CeO₂^{Com}, (c) 5Ni-CeO₂^{Imp}, (d) 2.5Ni-CeO₂^{*}, (e) 5Ni-CeO₂^{*} and (f) 10Ni-CeO₂^{*} catalysts.

nation method, which led to agglomeration of catalyst particles [5]. The analysis of BET-Surface area of spent catalysts revealed that the catalysts synthesized by here described method remained

Table 1
Physicochemical properties of different catalysts.

Catalyst	Surface Area (m ² /g)	Metal Dispersion (MD; %)	Avg. Particle Size (nm)						No. of surface Ni species/g catalyst (From MD)	
			From TEM		From XRD		From MD			
			CeO ₂	Nickel species	CeO ₂	Nickel species	Nickel species			
CeO ₂ [*]	68.3	NA	41.2	NA	42.2	NA	NA	NA	NA	
CeO ₂ ^{Com}	17.3	NA	118.4	NA	ND	NA	NA	NA	NA	
Fresh Catalyst										
2.5Ni-CeO ₂ [*]	72.6	27.4	41.6	4.6	42.0	ND	4.7	2.25×10^{15}		
5Ni-CeO ₂ [*]	75.8	24.6	42.0	5.6	41.8	5.7	5.5	3.06×10^{15}		
10Ni-CeO ₂ [*]	76.3	17.3	41.4	7.7	41.9	8.2	8.2	2.20×10^{15}		
5Ni-CeO ₂ ^{Imp}	16.5	2.6	ND	ND	ND	ND	33.2	1.25×10^{13}		
5Ni-CeO ₂ ^{Com}	18.2	4.9	120.2	27.1	ND	ND	26.3	3.39×10^{13}		
Spent Catalyst										
2.5Ni-CeO ₂ [*]	70.4	ND	42.4	4.3	42.3	ND	ND	ND		
5Ni-CeO ₂ [*]	72.7	ND	42.1	5.4	41.9	5.6	ND	ND		
10Ni-CeO ₂ [*]	70.5	ND	41.7	7.9	41.8	8.1	ND	ND		
5Ni-CeO ₂ ^{Imp}	9.4	ND	ND	ND	ND	ND	ND	ND		
5Ni-CeO ₂ ^{Com}	5.6	ND	ND	ND	ND	ND	ND	ND		

ND: Not determined. NA: Not applicable.

Spent catalyst condition: Reaction time (20 h, TOS), Temperature (800 °C), Pressure (1 atm), WHSV (80,000 mg l⁻¹ h⁻¹), Feed ratio (O₂:CH₄:He = 1:2:8.5).

Table 2

H_2 -consumption during H_2 -TPR analysis of Ni-CeO₂ catalysts.

Catalyst	Temperature (°C)	H_2 -consumption values (mmol/g)		
		Expected for Ni-oxide	Experimental	due to surface oxygen of CeO ₂
2.5Ni- CeO ₂ *	200–550	0.4259	1.3542	0.9283
5Ni- CeO ₂ *	200–550	0.8519	1.5673	0.7154
10Ni- CeO ₂ *	200–550	1.7038	1.9746	0.2708
5Ni-CeO ₂ ^{Com}	320–500	0.8519	0.5435	0.00
5Ni-CeO ₂ ^{Imp}	300–520	0.8519	0.6652	0.00

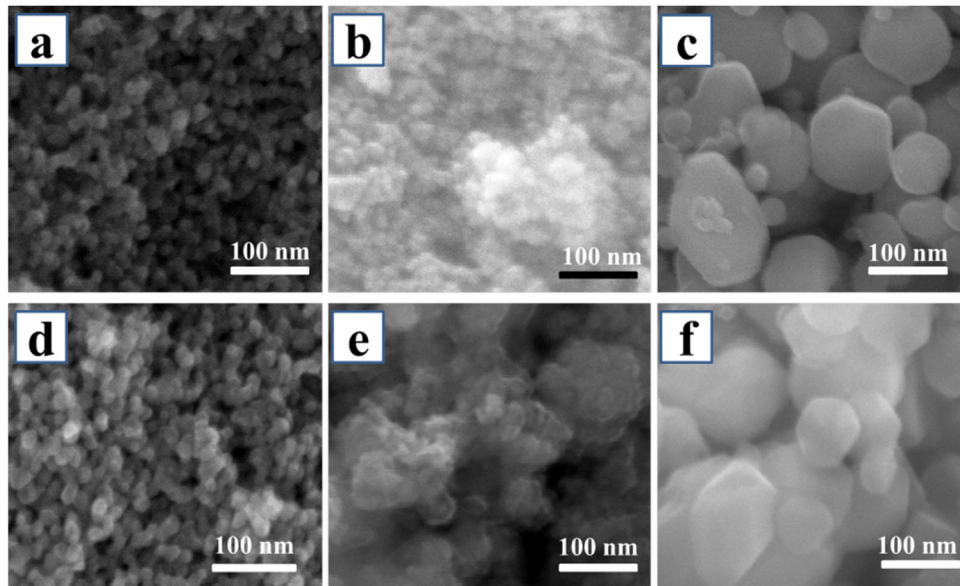


Fig. 3. SEM images of fresh (a) 5Ni-CeO₂*; (b) 5Ni-CeO₂^{Imp}; (c) 5Ni-CeO₂^{Com} and spent (d) 5Ni-CeO₂*; (e) 5Ni-CeO₂^{Imp} and (f) 5Ni-CeO₂^{Com} catalysts. Spent catalyst condition: Reaction time (20 h, TOS), Temperature (800 °C), Pressure (1 atm), WHSV (80,000 mlg⁻¹ h⁻¹), Feed ratio (O₂:CH₄:He = 1:2:8.5).

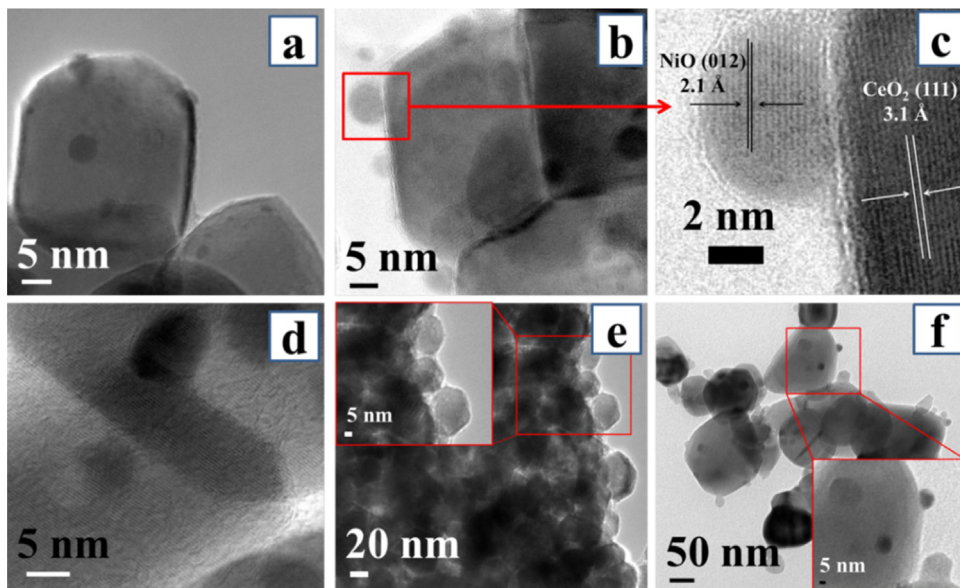


Fig. 4. TEM images of fresh (a) 2.5Ni-CeO₂*; (b) 5Ni-CeO₂*; (c) HR-TEM image of 5Ni-CeO₂*; (d) 10Ni-CeO₂*; (e) 5Ni-CeO₂^{Imp} and (f) 5Ni-CeO₂^{Com} catalysts.

unaffected (Table 1). The unaffected physical properties of catalyst indicated metal-support interactions in the catalysts, which prevented sintering of catalyst particles [4,5,24]. The analysis of spent catalysts by XRD (Fig. 1) and TEM (Fig. 5) also showed unchanged physical properties of the catalysts synthesized by here described

method (Table 1). However, the catalyst synthesized by impregnation method showed further decrease in surface area due to further agglomeration of catalyst particles during catalysis. The decrease in surface area for 5Ni-CeO₂^{Imp} and 5Ni-CeO₂^{Com} catalyst could also be due to coke formation during catalysis (Fig. 8, Table 3).

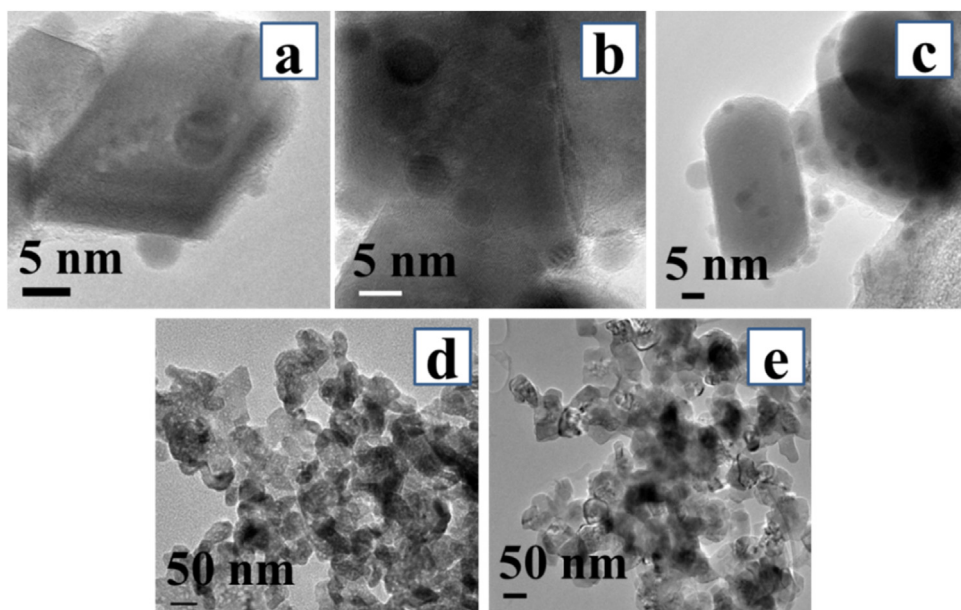


Fig. 5. TEM images of spent (a) 2.5Ni-CeO₂*; (b) 5Ni-CeO₂*; (c) 10Ni-CeO₂*; (d) 5Ni-CeO₂^{Imp} and (e) 5Ni-CeO₂^{Com} catalysts. Spent catalyst condition: Reaction time (20 h, TOS), Temperature (800 °C), Pressure (1 atm), WHSV (80,000 mg l⁻¹ h⁻¹), Feed ratio (O₂:CH₄:He = 1:2:8.5).

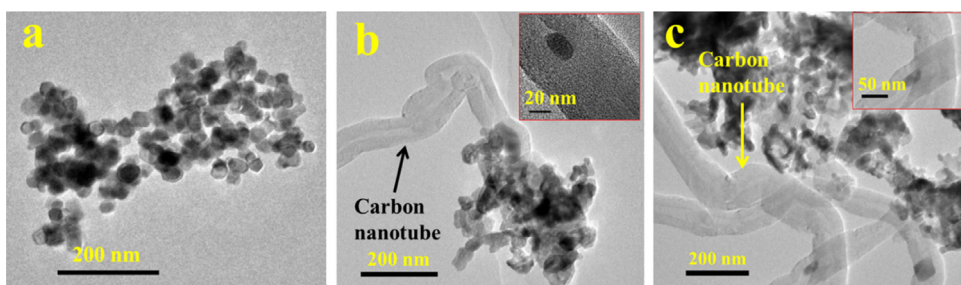


Fig. 6. Type of carbon deposited on spent (a) 5Ni-CeO₂*; (b) 5Ni-CeO₂^{Com}; and (c) 5Ni-CeO₂^{Imp} catalysts. Spent catalyst condition: Reaction time (20 h, TOS), Temperature (800 °C), Pressure (1 atm), WHSV (80,000 mg l⁻¹ h⁻¹), Feed ratio (O₂:CH₄:He = 1:2:8.5).

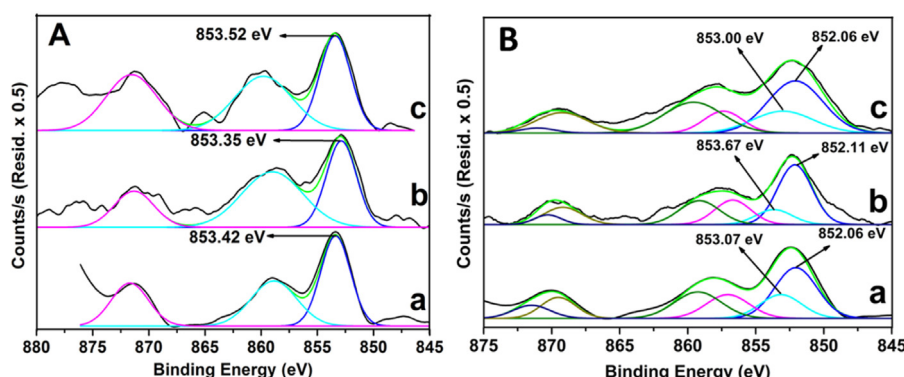


Fig. 7. Core level Ni2p XPS spectra of (A) fresh (a) 5Ni-CeO₂*; (b) 5Ni-CeO₂^{Imp}; (c) 5Ni-CeO₂^{Com} and (B) spent (a) 5Ni-CeO₂*; (b) 5Ni-CeO₂^{Imp} and (c) 5Ni-CeO₂^{Com} catalysts. Spent catalyst condition: Reaction time (20 h, TOS), Temperature (800 °C), Pressure (1 atm), WHSV (80,000 mg l⁻¹ h⁻¹), Feed ratio (O₂:CH₄:He = 1:2:8.5).

Table 3
Type of deposited carbon on different catalysts.

Catalysts	CH _x + C _{g/n} (g/g cat)	CH _x (g/g cat)	C _{g/n} (g/g cat)	Ratio (CH _x :C _{g/n})
2.5Ni-CeO ₂ *	0.0094	0.0089	0.0005	17.8
5Ni-CeO ₂ *	0.0180	0.0120	0.0060	2.0
10Ni-CeO ₂ *	0.0466	0.0286	0.018	1.588
5Ni-CeO ₂ ^{Com}	0.0560	0.017	0.039	0.436
5Ni-CeO ₂ ^{Imp}	0.0510	0.004	0.047	0.045

Note: (CH_x) → Hydrogen containing carbon species.
(C_{g/n}) → Graphitic carbon or carbon nanotubes.

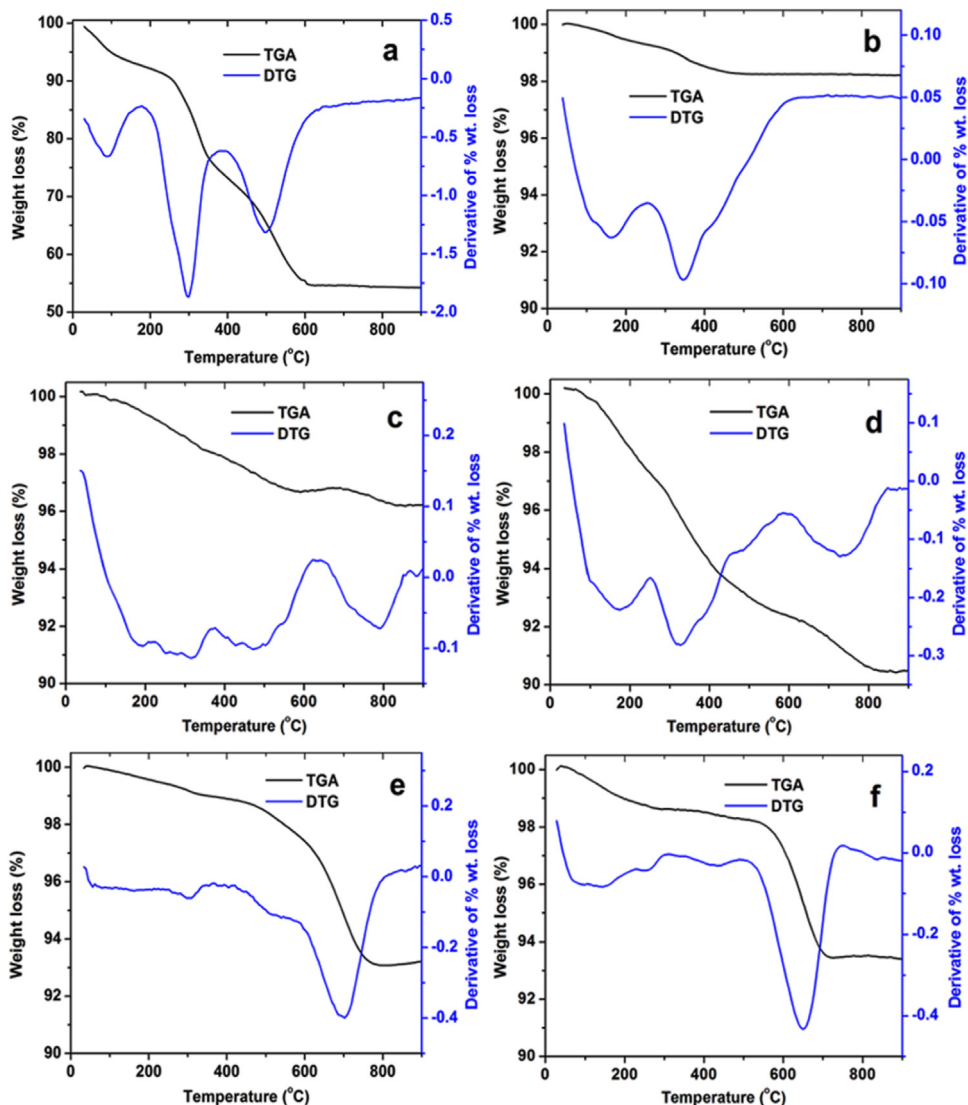


Fig. 8. TGA/DTG patterns of (a) uncalcined 5Ni-CeO₂^{*}, spent (b) 2.5Ni-CeO₂^{*}, (c) 5Ni-CeO₂^{*}, (d) 10Ni-CeO₂^{*}, (e) 5Ni-CeO₂^{Com} and (f) 5Ni-CeO₂^{Imp} catalysts. Spent catalyst condition: Reaction time (20 h), TOS, Temperature (800 °C), Pressure (1 atm), WHSV (80,000 mg g⁻¹ h⁻¹), Feed ratio (O₂:CH₄:He = 1:2:8.5).

3.1.2. Metal dispersion

H₂-chemisorption analysis was carried out with a mixture of 10%H₂ and 90%He gas to find out the average number of nickel species present on catalyst surface. Table 1 shows nickel species dispersion, nickel species size and number of nickel species present per gram catalyst, obtained from metal dispersion analysis. The obtained results showed that nickel species dispersion was dependent on support surface area, method of nickel loading and amount of nickel loading [4,5,24]. The catalysts synthesized by here described method showed much better nickel species dispersion with smaller nickel species sizes, whereas the catalyst synthesized by impregnating nickel showed much lower nickel species dispersion with higher nickel species size. The reason was the use of morphology controlling agent CTAB and size controlling agent PVP as described in the synthesis procedure, which enhanced nickel species dispersion by controlling size and shape of the nickel species but absence of such morphology and size controlling agent during impregnation of nickel of Ni-CeO₂^{Imp} catalyst, led to much bigger nickel species formation with lower dispersion [4,5,24]. 5Ni-CeO₂^{*} catalyst showed nickel species dispersion of 24.6% with average nickel species size 5.5 nm, whereas 5Ni-CeO₂^{Imp} catalyst showed metal dispersion of only 2.6% with average nickel

species size 33.2 nm. So, the obtained results revealed that method for nickel loading played the most important role for nickel species formation and its distribution over catalyst surface [4,5,24]. It was observed that the nickel species dispersion for 5Ni-CeO₂^{Com} catalyst was 4.9% with average nickel species size 26.3 nm. In this case, the lower nickel species dispersion and higher nickel species size was the result of lower surface area of commercial CeO₂ [8,35].

5Ni-CeO₂^{*} with 5Ni-CeO₂^{Imp} catalysts were prepared using the same support but Ni-deposition was carried out by different procedures. First, 5Ni-CeO₂^{*} catalyst was prepared by depositing nickel over CeO₂^{*} support (68.3 m²/g), in presence of morphology controlling agent CTAB (controlled the spherical morphology of the nickel species) and PVP as a size controlling agent (for nickel species). Controlled deposition of nickel caused the formation of smaller nickel species and improved the Ni-dispersion (24.6%) [5,36]. But, for 5Ni-CeO₂^{Imp} catalyst, nickel was deposited over the same CeO₂^{*} support by conventional impregnation method. Uncontrolled deposition of nickel in absence of CTAB and PVP caused the formation of larger nickel species resulting in much lower nickel dispersion (2.6%) [5,36]. On the other hand, 5Ni-CeO₂^{Com} and 5Ni-CeO₂^{Imp} catalysts, showed almost similar Ni-dispersion despite using the controlled deposition process of nickel for 5Ni-CeO₂^{Com} catalyst.

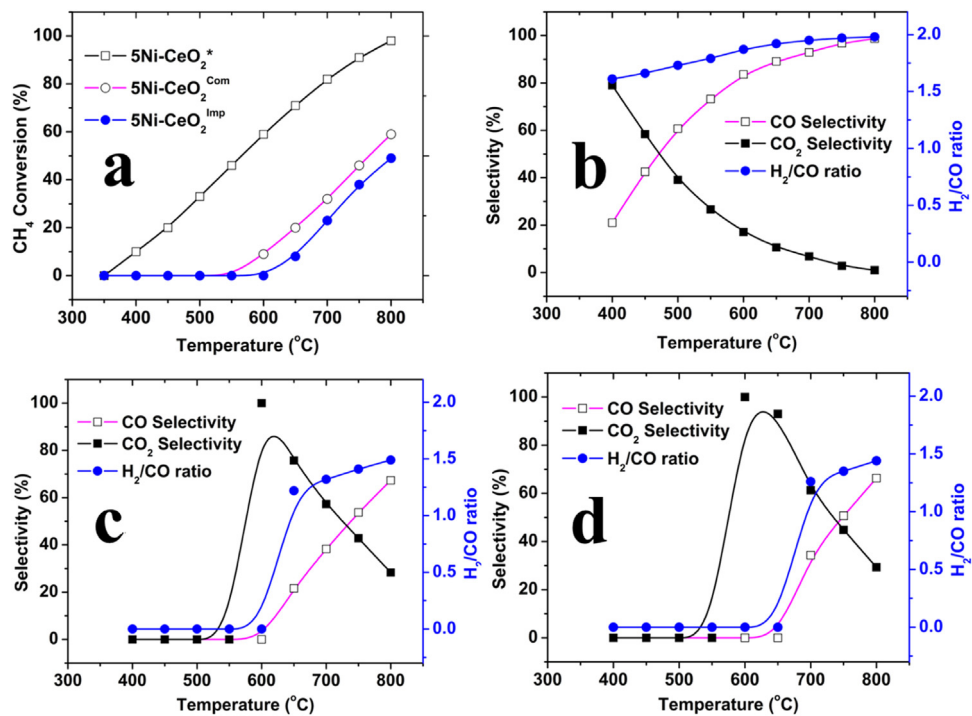


Fig. 9. (a) CH₄ conversion over different catalysts and product selectivity, H₂/CO ratio over (b) 5Ni-CeO₂^{*}, (c) 5Ni-CeO₂^{Com} and (d) 5Ni-CeO₂^{Imp} catalysts. Reaction Condition: Catalyst weight (60 mg), Reaction time (6 h), Temperature (350–800 °C), Pressure (1 atm), WHSV (80,000 mg g⁻¹ h⁻¹) and feed ratio (O₂:CH₄:He = 1:2:8.5).

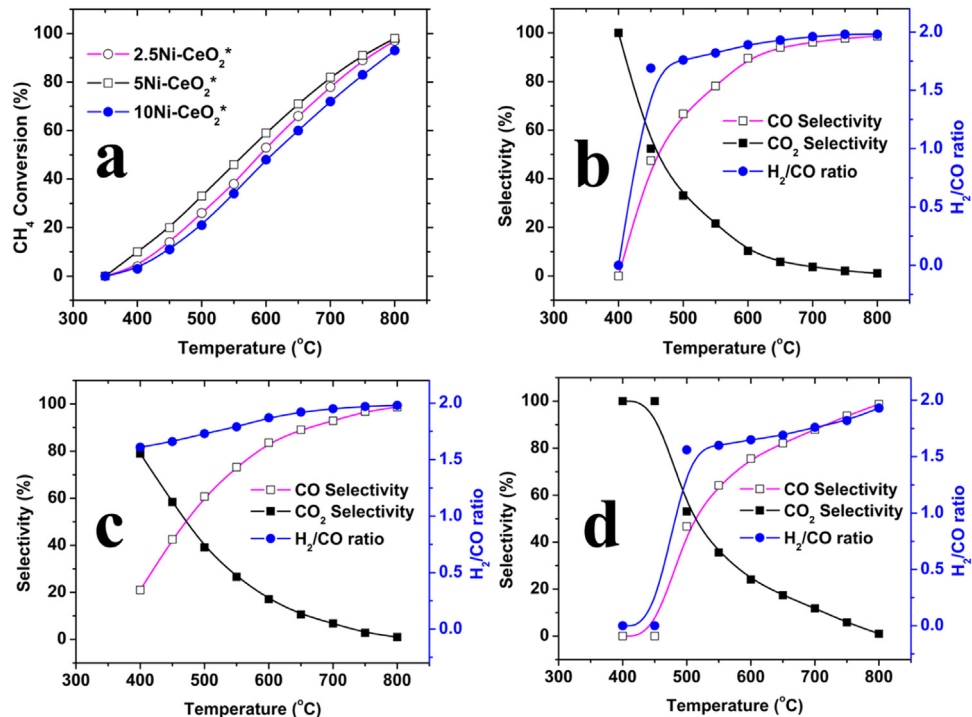


Fig. 10. Effect of Ni loading on (a) CH₄ conversion and product selectivity, H₂/CO ratio over (b) 2.5Ni-CeO₂^{*}, (c) 5Ni-CeO₂^{*}, (d) 10Ni-CeO₂^{*} catalysts. Reaction Condition: Catalyst weight (60 mg), Reaction time (6 h), Temperature (350–800 °C), Pressure (1 atm), WHSV (80,000 mg g⁻¹ h⁻¹) and feed ratio (O₂:CH₄:He = 1:2:8.5).

The observation can be explained by the fact that despite applying the controlled deposition process for nickel species, 5Ni-CeO₂^{Com} catalyst showed low Ni-dispersion due to low surface area of the commercial CeO₂ support (17.3 m²/g). Very low surface area of commercial CeO₂ increased the surface density of nickel species during nickel deposition and unavailability of support surface caused the formation of larger nickel species and the dispersion of

nickel species was low (4.9%) [37]. Obtained results indicated that Ni-dispersion was not only dependent on nickel deposition process but was also dependent on available surface for the dispersion of active species. We also calculated the number of nickel species/g catalyst for different catalysts. Depending on nickel species dispersion and nickel species size, number of nickel species present in the catalysts also varied. Number of average nickel species per

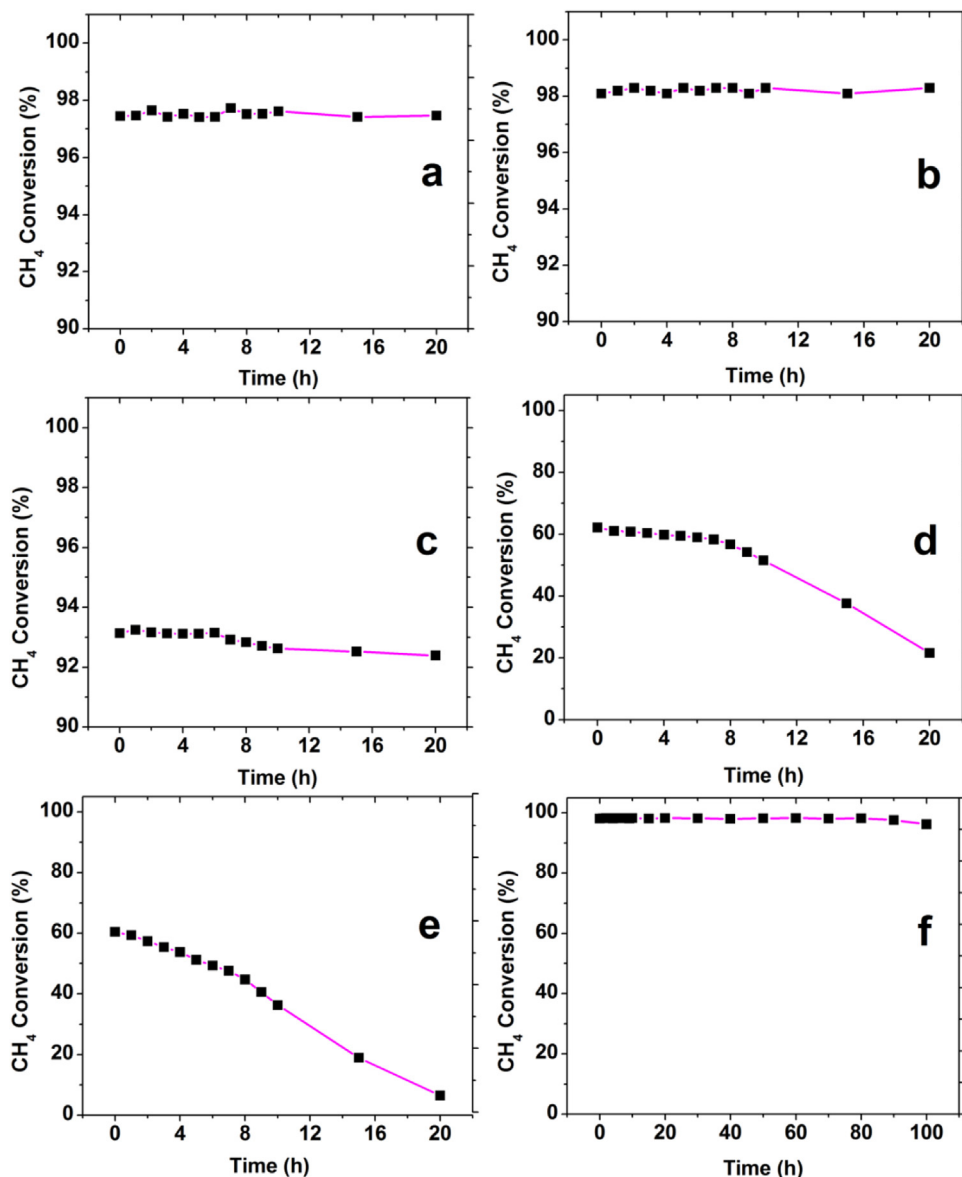


Fig. 11. 20 h Time on stream (TOS) for (a) 2.5Ni-CeO₂^{*}, (b) 5Ni-CeO₂^{*}, (c) 10Ni-CeO₂^{*}, (d) 5Ni-CeO₂^{Com}, (e) 5Ni-CeO₂^{Imp} catalysts and (f) 100 h TOS for 5Ni-CeO₂^{*} catalyst. Reaction Condition: Catalyst weight (60 mg), Temperature (800 °C), Pressure (1 atm), WHSV (80,000 ml g⁻¹ h⁻¹) and feed ratio (O₂:CH₄:He = 1:2:8.5).

gram catalyst was calculated from average nickel particle size and the active metal (nickel) surface area obtained from metal dispersion results. Considering the spherical nature of the nickel species (also evident from TEM analysis), number of average nickel species can be calculated from active metallic surface area [8]. The catalysts with higher Ni dispersion, as obtained from the analysis of metal dispersions, indicated better metal support interaction [38].

3.1.3. XRD measurements

Powder X-ray diffraction (XRD) patterns of the synthesized fresh catalysts are presented in Fig. 1A. Fig. 1Aa shows the reference XRD peaks of NiO (JCPDS Card 22-1189). All the Ni-CeO₂ catalysts showed characteristic XRD peaks for cubic CeO₂ (JCPDS Card 81-0792). Fresh 5Ni-CeO₂^{Com} and 5Ni-CeO₂^{Imp} catalysts showed presence of NiO peaks at 2θ values of 37.2°, 43.3°, 62.9° and 75.4° (Fig. 1Ab and Ac). 2.5Ni-CeO₂^{*} catalyst (Fig. 1Ad) showed no sign of NiO peaks in its XRD pattern because of low loading and highly dispersed Ni species with very small particle size [39,40] as XRD is a bulk sensitive technique and it requires crystallites with above 3 nm to detect but some literature also mentioned that detec-

tion of below 5 nm crystallites are not possible by XRD [4,5] or it could be possible that amorphous nickel species were present in the catalyst. 5Ni-CeO₂^{*} catalyst (Fig. 1Ae) showed a very small peak for NiO and the intensity of NiO peak was increased for 10Ni-CeO₂^{*} catalyst (Fig. 1Af). The reason may be the formation of larger NiO particles [41] with increasing Ni loading, as with increasing Ni loading, dispersion of the Ni species decreased (Table 1). The results obtained from metal dispersion analysis were also in agreement with the observation from XRD patterns of Ni-CeO₂^{*} catalysts (Fig. 1Ad–Af). Average Ni-species size for 2.5Ni-CeO₂^{*}, 5Ni-CeO₂^{*}, 10Ni-CeO₂^{*}, 5Ni-CeO₂^{Com} and 5Ni-CeO₂^{Imp} catalysts were 4.7 nm, 5.5 nm, 8.2 nm, 26.3 nm and 33.2 nm, respectively (Table 1). The 5Ni-CeO₂^{Com} and 5Ni-CeO₂^{Imp} catalyst also showed NiO peak as a result of larger NiO particles with low dispersion [4,5,24]. The NiO peaks at 2θ values 37.2°, 43.3° and 62.88° are attributed to (003), (012) and (104 or 110) planes respectively (JCPDS Card 22-1189).

XRD analysis for the spent catalysts was also performed to check the reaction condition effect on the catalysts phases. Fig. 1Ba–Bd and 1Be shows the XRD patterns for 2.5Ni-CeO₂^{*}, 5Ni-CeO₂^{*}, 10Ni-CeO₂^{*}, 5Ni-CeO₂^{Com} and 5Ni-CeO₂^{Imp} catalysts, respectively. All

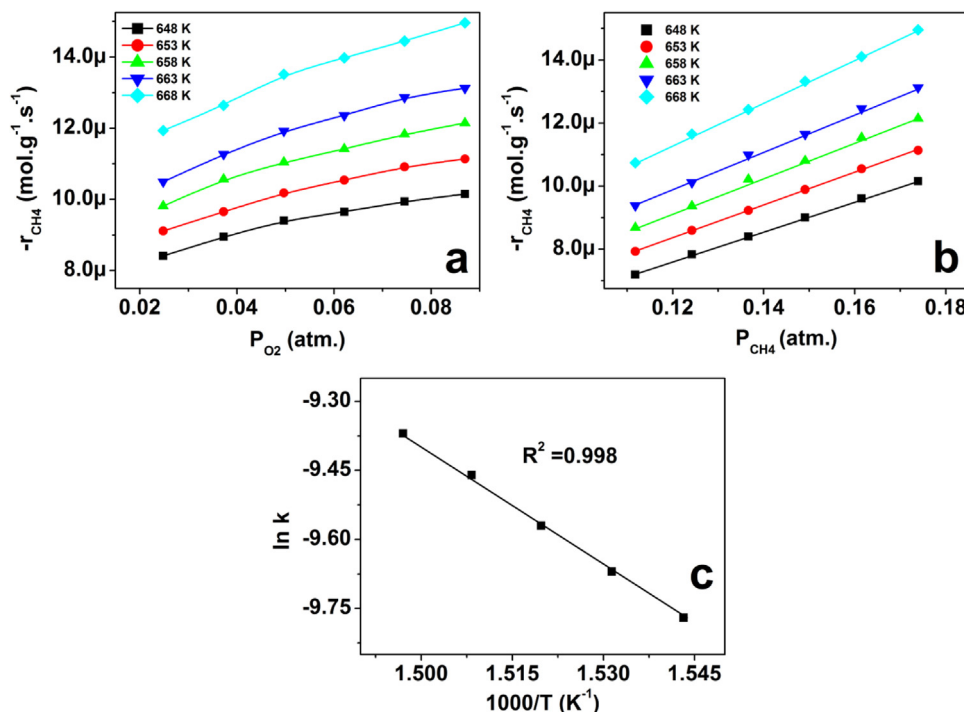


Fig. 12. (a) Change of rate with partial pressure of oxygen ($P_{CH_4} = 0.174$ atm), (b) change of rate with partial pressure of methane ($P_{O_2} = 0.087$ atm) and (c) Plot of $\ln k$ vs $1000/T$ for 5Ni-CeO₂* catalyst.

the catalysts showed peaks for unchanged CeO₂ cubic phase, indicating the thermal stability of cubic CeO₂ phase [5]. 10Ni-CeO₂*^{*}, 5Ni-CeO₂^{Com} and 5Ni-CeO₂^{Imp} catalysts also showed a peak at 2θ value of 26.6° (Fig. 1Bc–Be), which was attributed to graphitic carbon (JCPDS Card 75-1621) deposited on the catalysts surface during catalysis [10,42,43]. Surprisingly, 2.5Ni-CeO₂* and 5Ni-CeO₂* catalysts showed no peak for graphitic carbon may be due to deposition of very low amount of carbon on surface catalyst during catalysis or due to the deposition of amorphous carbon species. TGA analysis also proved very low carbon deposition on spent 2.5Ni-CeO₂* and 5Ni-CeO₂* catalysts (discussed later). Spent 5Ni-CeO₂* and 10Ni-CeO₂* catalysts showed a XRD peak of metallic nickel at 2θ value 44.5°, whereas 5Ni-CeO₂^{Com} and 5Ni-CeO₂^{Imp} catalysts showed two XRD peaks of metallic nickel at 2θ values 44.5° and 51.8° (JCPDS Card 04-0850), but spent 2.5Ni-CeO₂* catalyst showed no peak for metallic nickel due to low loading and smaller nickel particle size unaffected even after the reaction, suggesting strong metal support interaction [8]. We strongly believe that low loading, high dispersion, smaller nickel species size (<5 nm) and strong metal support interaction between nickel particles and CeO₂* particles inhibited sintering of nickel nanoparticles during catalysis. It can be seen from the several experimental analysis that fresh 2.5Ni-CeO₂* catalyst contains nickel species with sizes <5 nm. Now, during catalysis strong metal (Ni)-support (CeO₂*^{*}) interaction resisted the agglomeration of nickel nanoparticles, keeping the size of metallic nickel below 5 nm. These nickel nanoparticles are not detectable by XRD technique [44–47] and the peaks for metallic nickel was absent for spent 2.5Ni-CeO₂* catalyst [48–50].

3.1.4. TPR measurements

Reducibility of catalysts particles were examined by H₂-TPR analysis with 10%H₂ balance He gas, as catalytic activity also depends on catalysts reducibility (discussed latter) [26]. Fig. 2a-f represents H₂-TPR pattern of CeO₂^{*}, 5Ni-CeO₂^{Com}, 5Ni-CeO₂^{Imp}, 2.5Ni-CeO₂^{*}, 5Ni-CeO₂^{*} and 10Ni-CeO₂^{*} catalysts, respectively. Reduction of pure cerium oxide (Fig. 2a) showed a reduction peaks

at about 520 °C and a broad peak starting from 680 °C to higher temperature [5]. The low temperature reduction was attributed to surface oxygen reduction of CeO₂ and at the high temperature, bulk cerium oxide reduction took place [22,51]. The catalyst particles with smaller crystallites showed nickel species and surface oxygen reduction at lower temperatures (Fig. 2), which was due to better redox properties of corresponding catalyst [32]. 5Ni-CeO₂^{Com} catalyst showed a reduction peak at 398 °C (Fig. 2b), which was attributed to reduction of nickel oxide species of the catalyst. 5Ni-CeO₂^{Imp} catalyst (Fig. 2c) showed a broad peak ranging from 290 to 500 °C for the reduction of larger nickel species crystals. The lower temperature broad peak of 5Ni-CeO₂^{Imp} catalyst was because of different sized particles formed during uncontrolled deposition of nickel by impregnation method i.e. different sized nickel species are reducible at different temperatures and the reduction pattern becomes broad [52] and of low intensity [4,5,24]. Agglomeration of catalyst particles hinders the exposure of nickel species during TPR analysis, which takes more time and temperature for reduction of particles [4,5,24,52]. Reduction of larger nickel oxide species formed due to agglomeration also inhibited the reduction of core nickel species of nickel oxide particles by the diffusion of hydrogen molecules, as the core species are not readily exposed to hydrogen for reduction [53]. 2.5Ni-CeO₂^{*}, 5Ni-CeO₂^{*} and 10Ni-CeO₂^{*} catalysts showed same reduction pattern during H₂-TPR analysis. Metal support interaction of Ni-CeO₂^{*} catalysts was confirmed from the H₂-TPR analysis (Fig. 2). Deconvolution of Ni-oxide reduction peaks in TPR analysis of Ni-CeO₂^{*} catalysts showed multiple peaks (e.g. 251 °C, 295 °C, 347 °C and 392 °C for 2.5Ni-CeO₂^{*}), which is the indication of different extent of metal (Ni)-support (CeO₂^{*}) interactions in Ni-CeO₂^{*} catalysts. Different metal-support interactions affected the reducibility of Ni-oxide particles [5,24,54]. Similar metal-support interaction was also explained in our earlier reports [4,5], where we showed that the smaller particles, which create better metal-support interactions get reduced at lower temperatures and were supported by the analysis of catalyst characterizations and catalytic results. Most

Table 4
Catalytic activities of different catalysts.

Entry	Catalyst	Ni wt%	Ignition temp. (°C)	Catalytic activity			
				Temp. (°C)	CH ₄ conv. (%)	H ₂ /CO ratio	Rate of CO formation (mol g ⁻¹ s ⁻¹)
1	NiO	100	800	800	19	0	ND
2	CeO ₂ *	0	800	800	11	1.6	ND
3	2.5Ni-CeO ₂ *	2.5	400	800	97	1.98	9.49 × 10 ⁻⁵
4	5Ni-CeO ₂ *	5	400	800	98	1.98	9.59 × 10 ⁻⁵
5	10Ni-CeO ₂ *	10	400	800	93	1.93	9.11 × 10 ⁻⁵
6	5Ni-CeO ₂ ^{Com}	5	600	800	59	1.49	3.94 × 10 ⁻⁵
7	5Ni-CeO ₂ ^{Imp}	5	650	800	49	1.44	3.22 × 10 ⁻⁵

Reaction condition: Reaction time (6 h), Catalyst wt. (60 mg), Pressure (1 atm), WHSV (80,000 ml g⁻¹ h⁻¹), Feed ratio (O₂:CH₄:He = 1:2:8.5).

Note: ND (Not determined).

intense Ni-oxide reduction peaks for 2.5Ni-CeO₂* , 5Ni-CeO₂* and 10Ni-CeO₂* catalysts were 347 °C, 362 °C and 383 °C (Fig. 2d-f). With increasing Ni loading, the reduction temperature of nickel oxide species shifted towards higher temperature, as larger nickel oxide crystals were not easily reduced [40,55,56].

Among 5Ni-CeO₂^{Com}, 5Ni-CeO₂^{Imp} and 5Ni-CeO₂* catalysts, 5Ni-CeO₂* catalyst showed much easily reducible nickel oxide particles and the TPR pattern indicated much better metal support interaction [4,5]. Table 2 shows the consumption of hydrogen during H₂-TPR analysis of different Ni-loaded catalysts. Total consumption of hydrogen showed that surface oxygen of cerium oxide also gets reduced at this temperature. Venezia et al. [32] reported that small variation in particles size and support surface changes the redox property of catalyst and the hydrogen consumption values for different catalysts also revealed that redox property of catalysts changed here. It can be seen that Ni-CeO₂* catalysts, with different Ni-loading showed different amount of surface oxygen reduction (Table 2), due to the change in Ni-crystallite size and surface area of the catalysts (Table 1) [32]. The possible amount of hydrogen consumption for surface oxygen of CeO₂* of 2.5Ni-CeO₂*, 5Ni-CeO₂* and 10Ni-CeO₂* catalysts were 0.9283 mmol/g, 0.7154 mmol/g and 0.2708 mmol/g, respectively. It can also be seen that for 5Ni-CeO₂^{Com} and 5Ni-CeO₂^{Imp} catalyst consumption of hydrogen was comparatively low. Hydrogen consumption of both 5Ni-CeO₂^{Com} and 5Ni-CeO₂^{Imp} catalysts showed that at the temperature range 320–500 °C and 300–520 °C for the respective catalysts, surface oxygen of support (CeO₂) was not reduced and Ni-oxide species was not completely reduced. Although, at slightly higher temperature (about 550 °C) both the catalyst showed a small reduction peak (Fig. 2b and c) but it could be due to the remaining nickel species and/or surface oxygen of support (CeO₂). Larger CeO₂^{Com} crystal and agglomerated CeO₂* crystals of 5Ni-CeO₂^{Com} and 5Ni-CeO₂^{Imp} catalyst reduced OSC of these catalysts and the consumption of hydrogen also reduced (Table 2) [5].

3.1.5. SEM and TEM measurements

Morphologies of fresh and spent 5Ni-CeO₂*, 5Ni-CeO₂^{Com} and 5Ni-CeO₂^{Imp} catalysts were checked by SEM analysis. SEM image of fresh 5Ni-CeO₂* catalyst (Fig. 3a) showed 30–50 nm catalyst particles, 5Ni-CeO₂^{Com} (Fig. 3b) showed much bigger and non-uniform sized catalyst particles (20–170 nm) and 5Ni-CeO₂^{Imp} catalyst (Fig. 3c) showed 30–50 nm catalyst particles in agglomerated form. So, the morphological differences can be clearly seen from the SEM images of different catalysts. The SEM images of different Ni-CeO₂* catalysts showed no significant difference (Supporting information Fig. S2). We also examined the morphologies of spent catalysts by SEM analysis. SEM image of spent 5Ni-CeO₂* catalyst (Fig. 3d) showed unchanged morphology and particle size (30–50 nm), whereas spent 5Ni-CeO₂^{Com} and 5Ni-CeO₂^{Imp} catalysts (Fig. 3e and f) showed agglomerated and sintered catalyst particle after catalysis. The actual catalysts particle sizes of spent 5Ni-CeO₂^{Com} and 5Ni-CeO₂^{Imp} catalysts could not be measured by

SEM analysis due to agglomeration and sintering. The unchanged morphology of spent 5Ni-CeO₂* catalyst was the result of high metal support interaction, which inhibited sintering of catalyst particles [4,5,24], but in case of 5Ni-CeO₂^{Imp} and 5Ni-CeO₂^{Com} catalysts, absence or weak metal support interaction, caused by agglomerated and bigger catalyst particles for the respective catalysts resulted the sintering of these catalyst particles [8]. The obtained results indicated that the synthesis method of catalysts played crucial role for morphology, metal support interaction and thermal stability of the catalyst [4,5,24].

Morphologies of the fresh catalysts were also checked by TEM and presented in Fig. 4. Table 1 depicts the particle size obtained from TEM analysis. TEM images of Ni-CeO₂* catalysts showed 30–50 nm CeO₂ crystals and spherical nickel species and SAED pattern showed polycrystalline nature of the catalyst (Supporting information Fig. S3). TEM images also showed increase in nickel species size with increasing nickel loading, TEM image of 2.5Ni-CeO₂* catalyst (Fig. 4a) showed average of 4.6 nm nickel species, 5Ni-CeO₂* catalyst (Fig. 4b) showed average 5.6 nm nickel species (Supporting information Fig. S4), whereas 10Ni-CeO₂* catalyst (Fig. 4d) showed average 7.7 nm of nickel species. The results were also in agreement with the species size obtained from metal dispersion analysis (Table 1). Fig. 4c shows the HR-TEM image of 5Ni-CeO₂* catalyst, fringes with d-spacing 2.1 Å was attributed to (012) plane of NiO, whereas the fringe with 3.1 Å was attributed to (111) plane of CeO₂ crystals. TEM image of 5Ni-CeO₂^{Imp} catalyst (Fig. 4e) showed 30–50 nm catalyst particles in agglomerated form, whereas 5Ni-CeO₂^{Com} catalyst (Fig. 4f) showed much bigger CeO₂ (50–170 nm) and nickel species of average 27.1 nm. Much larger nickel species of 5Ni-CeO₂^{Com} catalyst was the result of low surface area of the support CeO₂^{Com} [37]. Elemental mapping of fresh 5Ni-CeO₂* catalyst showed uniform distribution of nickel species (Supporting information Fig. S5).

To check the reaction condition effect on morphologies of all the catalysts, TEM analysis of spent catalysts were carried out. The TEM images of spent 2.5Ni-CeO₂*, 5Ni-CeO₂*, 10Ni-CeO₂*, 5Ni-CeO₂^{Imp} and 5Ni-CeO₂^{Com} catalysts are shown in Fig. 5a–e, respectively. Spent 2.5Ni-CeO₂* and 5Ni-CeO₂* catalysts (Fig. 5a and b) showed absolutely no sintering or agglomeration of catalyst particles, whereas spent 10Ni-CeO₂* catalyst (Fig. 5c) showed just a hint of agglomeration of catalyst particles may be due to comparatively larger nickel species sizes than the nickel species sizes in 2.5Ni-CeO₂* and 5Ni-CeO₂* catalysts, as with increase in nickel species size the metal support interaction between nickel species and CeO₂* nanoparticles decreased [38]. Now, comparison of spent 5Ni-CeO₂^{Imp} and 5Ni-CeO₂^{Com} catalysts with spent 5Ni-CeO₂* catalyst shows clear differences in the TEM images. Spent 5Ni-CeO₂^{Imp} and 5Ni-CeO₂^{Com} catalysts (Fig. 5d and e) showed sintering of catalysts particles due to low metal support interactions during catalysis [4,5,24]. Spent 5Ni-CeO₂* catalyst showed about average 5.4 nm nickel species, whereas due to sintering the measurement of catalyst particles for spent 5Ni-CeO₂^{Imp} and 5Ni-CeO₂^{Com} cata-

Table 5CH₄ conversion temperature for different catalysts (from Figs. 9 and 10).

Catalyst	T10% (°C)	T50% (°C)	T90% (°C)
2.5Ni-CeO ₂ *	425	591	761
5Ni-CeO ₂ *	400	568	750
10Ni-CeO ₂ *	445	609	787
5Ni-CeO ₂ ^{Com}	605	764	ND
5Ni-CeO ₂ ^{Imp}	655	800	ND

Note: TX → Temperature at which CH₄ conversion is X%.

ND → Not determined, as maximum reaction temperature experimented was 800 °C.

Table 6

Kinetic parameters used in Fig. 12.

Temperature (K)	−r _{CH4} = k.(P _{CH4}) ^B .(P _{O2}) ^C		
	k	B	C
648	5.71 × 10 ⁻⁵	0.781	0.149
653	6.31 × 10 ⁻⁵	0.774	0.163
658	6.98 × 10 ⁻⁵	0.768	0.169
663	7.79 × 10 ⁻⁵	0.757	0.180
668	8.52 × 10 ⁻⁵	0.741	0.183

lysts was not possible. Therefore, the TEM images of spent catalysts also showed the effect of catalyst preparation method for its catalytic activity and stability. We have also carried out TEM analysis for the deposited carbon on different catalyst surface (Fig. 6). TEM analysis for the deposited carbon revealed carbon nanotubes over spent 5Ni-CeO₂^{Com} and spent 5Ni-CeO₂^{Imp} catalysts (Fig. 6b and c). From the TEM images of spent 5Ni-CeO₂* catalyst (Fig. 6a), the type of carbon was not confirmed, may be because of amorphous nature of deposited carbon and/or the deposited graphitic carbon or carbon nanotubes was very low (0.6 wt%), which was not detected by the TEM images.

3.1.6. XPS measurements

Surface analyses for the nickel species present on different catalyst surface were performed by X-ray photoelectron spectroscopy (XPS). Fig. 7A and B represents the core level Ni2p XPS spectra of fresh and spent catalysts. All the fresh catalyst, independent of preparation methods showed pure NiO on catalysts surface. Ni2p_{3/2} XPS peaks with binding energy values of 853.42 eV, 853.35 eV and 853.52 eV confirmed NiO on surfaces of fresh 5Ni-CeO₂*, 5Ni-CeO₂^{Imp}, 5Ni-CeO₂^{Com} catalysts (Fig. 7Aa–Ac). The XPS analyses of spent catalysts showed the presence of metallic nickel and NiO in all the catalysts. The Ni2p_{3/2} XPS peak at binding energy values of 852.06 eV, 852.11 eV and 852.06 eV confirmed metallic nickel and XPS peaks at binding energy values 853.07 eV, 853.67 eV and 853.00 eV confirmed NiO species in spent 5Ni-CeO₂*, 5Ni-CeO₂^{Imp}, 5Ni-CeO₂^{Com} catalysts (Fig. 7Ba–Bc) respectively. The presence of NiO was not detected by XRD of the spent catalysts may be due to small size and/or small amount. Presence of metallic nickel on spent catalyst surfaces was the result of activation process and the in-situ reduction of nickel oxides (produced by re-oxidation of the metallic nickel species) by the produced hydrogen during catalysis [4,5,24].

3.1.7. TGA/DTG analysis

Thermal stability of 5Ni-CeO₂* catalyst was checked by TGA analysis of uncalcined sample in presence of air (Fig. 8a). Three distinct weight loss regions were observed for the uncalcined 5Ni-CeO₂* catalyst. 1st weight loss at temperature 50–220 °C attributed to loss of adsorbed water, the 2nd weight loss at 220–320 °C was because of decomposition of hydroxides releasing water molecules and the third weight loss at 310–605 °C was attributed to loss of carbon species like CTAB and PVP, present in catalyst [57].

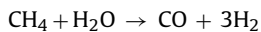
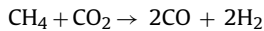
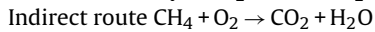
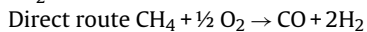
We also carried out TGA/DTG analysis of all the spent catalysts to find out the nature and percentage of carbon deposited on different catalyst surfaces. Literature reports suggested that the hydrogen containing carbon species (CH_x) is removable below 600 °C and graphitic carbon is removable only above 600 °C [4,24,32], as the gasification of CH_x species is much easier than the solid carbon. TGA analysis of spent 2.5Ni-CeO₂* catalyst (Fig. 8b) showed only 1.7% weight loss in the temperature region between 50 and 550 °C and the DTG analysis showed that it was the result of loss of adsorbed water and the loss of hydrogen containing carbon species (CH_{x(x=1–3)}) [4,24,53]. Above 550 °C, no weight loss was observed. The observed result indicated excellent coke resistivity of the catalyst. This was mainly because of very high metal support interaction between less than 5 nm of nickel species with the support CeO₂* nanoparticles [8,38]. TGA analysis of spent 5Ni-CeO₂* catalyst (Fig. 8c) showed total 3.8% weight loss in the temperature region between 50 and 900 °C. The TGA plot showed two weight loss regions; first loss was from 50 to 620 °C and second loss was from 700 to 870 °C, whereas a closer look from the DTG plot showed three different weight loss regions. The first weight loss (2 wt%) from 50 to 360 °C, the second weight loss (1.2 wt%) was from 360 to 620 °C and the third weight loss was between 700 and 870 °C. The third weight loss (0.6%) was attributed to loss of deposited carbon as graphitic carbon [11,38,42,58,59]. TGA/DTG analysis of spent 10Ni-CeO₂* catalyst (Fig. 8d) also showed similar weight loss regions with total loss of 9.6% of which, 1.8% loss was due to loss of deposited graphitic carbon and/or carbon nanotubes as CO or CO₂ at temperature region 600–850 °C [4,5,24,53,60]. Increase in nickel species size led to such kind of observation from the TGA/DTG analysis of Ni-CeO₂* catalysts, because increase in metal particle size led to less metal support interaction between nickel species and support CeO₂* nanoparticles [38]. Therefore, with increase in nickel species size, the type and the percentage of deposited carbon was also varied [4,24,53].

The TGA/DTG plot of spent 5Ni-CeO₂^{Com} catalyst (Fig. 8e) showed 7% weight loss in the temperature between 50 and 900 °C of which, 1.7 wt% losses was for hydrogen containing carbon species and 3.9 wt% loss was because of loss of graphitic carbon and/or carbon nanotubes (Fig. 6b) [11,38,42,58,59]. CH_x species was removed below 600 °C and the graphitic carbon or carbon nanotubes were removed above 600 °C. TGA/DTG analysis of 5Ni-CeO₂^{Imp} catalyst (Fig. 8f) showed 6.5% of total weight loss with 0.4% loss due to hydrogen containing carbon species and 4.7% loss was the result of loss of graphitic carbon and/or carbon nanotubes (Fig. 6c) [11,38,42,58,59]. Recently, Venezia and her group [32] reported that over smallest nickel particle maximum carbon deposition took place and the deposited carbon was oxidized below 600 °C during TGA analysis but the catalyst remained very stable during TOS. So, the deposited carbon which was removed below 600 °C, was not the reason of catalyst deactivation [4,24,32,53,60]. Therefore, from the TGA analysis it was clear that the type of deposited carbon also varies with the nature of nickel species and metal support interactions [4,24,53,60]. Table 3 shows the type and the respective amount of deposited carbon species on different catalysts. It can be seen that the CH_x to C_{g/n} ratio decreased with increasing Ni-species size i.e. graphitic carbon or carbon nanotube (C_{g/n}) deposition increased, whereas deposition of hydrogen containing carbon species (CH_x) decreased with increasing Ni-species size. The ratio of CH_x to C_{g/n} was decreased from 17.8 to 1.59, when nickel loading was increased from 2.5 wt% to 10 wt% for Ni-CeO₂* catalysts. Comparing the TGA/DTG plots, we can say that the nickel deposition method also has a significant role in carbon deposition on nickel surfaces during catalysis of POM [4,24,53]. So, the catalyst support and nickel species size is a very important factor to control carbon formation over catalyst surface [61–64].

3.2. Catalytic activity

The active species for POM reaction is metallic form of active particles [5,65–68]. Reducibility of the active particles depends on its size [40,55]. With increasing particles size, reducibility of the particles decreases [40,55,56], which affect POM activity of the catalyst. Different literature reports suggested that Ni-oxide favors the complete oxidation, whereas metallic nickel favors partial oxidation of methane [39,65,69,70]. Although, the catalytic activity of the catalysts were tested with reduced catalysts, during the initial stage of the reaction, metallic nickel particles can be re-oxidized to Ni-oxide species and complete oxidation of methane can be major reaction. Complete oxidation of methane is highly exothermic reaction and the generated heat can cause sintering of the catalysts particles and lower its activity [1,26]. The hydrogen species formed by the dissociation of methane on nickel species surface can again reduce the oxidized nickel species to its metallic form and favor POM. The smaller the nickel particle size, the easier will be to reduce it by the produced hydrogen (during catalysis) and will favor POM reaction [22].

Synthesis gas generation through POM can occur via direct or indirect route [5,71,72]. Now distinction between two routes is difficult, as CO and H₂ can be primary products or secondary products and the presence of CO₂ and H₂O do not imply the indirect route [5,21]. CO₂ and H₂O can be produced by further oxidation of CO and H₂.



All the methane reforming reactions are dependent on metal particles size [1,4,5,24]. Literature reports also suggest that smaller catalysts particles interact with each other strongly and create strong metal support interactions and provide higher metal-support interfacial surface area, which highly influence the activity of catalyst [4,5,24]. Smaller active particles are reported to be more active for POM reaction, whereas larger particles favor complete oxidation of methane [5,22]. So, the possibility of direct POM route will dominate in case of smaller particles as compared to larger active particles. Direct route is favorable as it is slightly exothermic as compared to indirect route [1]. Although, indirect route for POM process proceeds through two endothermic reactions, namely CO₂ reforming (dry reforming) of methane and steam reforming of methane but the first step of the indirect route is highly exothermic (complete oxidation of methane) [1,5]. So, during indirect mechanism of POM, the catalysts property can be destroyed by the generated heat during complete oxidation of methane before the formation of syngas via CO₂ reforming and steam reforming of methane [26]. So, smaller catalyst particles are desirable for better catalytic activity [1]. Due to highly exothermic nature, complete oxidation is favorable over POM at lower temperature [5,21]. If the reaction occurs via indirect route, at high space velocity there should be only combustion products CO₂ and H₂O [1]. Furthermore, indirect route proceeds via CO₂ reforming of methane and steam reforming of methane and at temperature below 600 °C, indirect route is highly unlikely [1]. Again, reports also suggested that POM occurs over metallic species, whereas oxidized species favors complete oxidation [69,70,73,74]. During catalysis there is always a possibility of re-oxidation of previously reduced particles as molecular oxygen is present during reaction. So, shifting of POM mechanism from direct to indirect route is also possible and is also reported in literature [75–77]. The direct route of POM reaction is more suitable for catalyst stability.

To analyze catalytic activity of Ni-CeO₂ catalysts, we have prepared 2.5Ni-CeO₂^{*}, 5Ni-CeO₂^{*}, 10Ni-CeO₂^{*}, 5Ni-CeO₂^{Com} and 5Ni-CeO₂^{Imp} catalysts and compared its catalytic activity in POM. From Table 4, it is clear that 5Ni-CeO₂^{*} catalysts showed superior activity compared to other catalysts. Although, 2.5Ni-CeO₂^{*} and 5Ni-CeO₂^{*} catalyst showed almost similar results but CO formation rate for 5Ni-CeO₂^{*} catalyst was little higher and 5 wt% Ni loading was optimum for the Ni-CeO₂^{*} catalysts. Catalytic activities of different catalysts varied with the catalyst particle sizes, number of particles per gram catalyst and metal support interactions. Similar rate for 2.5Ni-CeO₂^{*}, 5Ni-CeO₂^{*} and 10Ni-CeO₂^{*} catalysts were due to the fact that the reaction was controlled by Ni-CeO₂^{*} interfacial surface area rather than Ni-loading. Table 5 shows CH₄ conversion temperature (TX%; temperature at which CH₄ conversion is X%) for different catalysts (from Figs. 9 and 10). 5Ni-CeO₂^{*} catalysts showed syngas formation at 400 °C and at this much low temperature methane reforming reactions are very unlikely to occur because both CO₂ reforming and steam reforming of methane reactions are highly endothermic and requires much higher temperature to initialize these reforming reactions [4,5,21]. Now, possibility of water gas shift reaction is also there. WGS (water gas shift) reaction is exothermic, whereas RWGS (reverse water gas shift) reaction is endothermic. So, WGS is expected to occur at lower temperature but RWGS is more favored at higher temperature. The H₂/CO ratio over 5Ni-CeO₂^{*} catalyst at 400 °C, was 1.61 but occurrence of WGS would have led to very high H₂/CO ratio (over 2). So, lower H₂/CO ratio ruled out the occurrence of WGS. Now, RWGS reaction could have decreased the H₂/CO ratio and in fact the H₂/CO ratio was low but at this temperature (400 °C) RWGS is not possible. So, our experimental results indicated about the direct route for synthesis gas production by POM and it was also supported by earlier literature reports [5,26]. Turn over frequency (TOF) for the reaction at 800 °C over 5Ni-CeO₂^{*} catalyst was calculated to be $1.89 \times 10^4 \text{ s}^{-1}$. TOF calculations were done from the corresponding reaction rates. The reaction rates were measured from the conversion of methane and selectivity of CO in the reaction product at that particular temperature. The Carbon balance and material balance for the catalyst was in between 98 and 102%.

TOF = Number of CO molecules produced per single active site per unit time.

4. Discussion

4.1. Catalytic activity

The catalytic properties of a catalyst were tested varying different reaction parameters like catalyst preparation method (Fig. 9), temperature (Figs. 9 and 10), weight hourly space velocity (WHSV) (Supporting information Fig. S6) and amount of nickel (Ni) loading (Fig. 10). Time on stream stability (TOS) for all the catalyst (Fig. 11) were also checked and reported. The effects of nickel deposition methods and support properties on the activities of catalysts are shown in Fig. 9. Three types of catalysts were prepared and their catalytic activities were studied and compared in same reaction conditions. Fig. 9 shows methane conversion and H₂/CO ratio over the designated catalysts for POM reaction. Among 5Ni-CeO₂^{*}, 5Ni-CeO₂^{Imp} and 5Ni-CeO₂^{Com} catalysts, 5Ni-CeO₂^{*} catalyst showed superior catalytic results in respect to methane conversion (Fig. 9a) and H₂/CO ratio (Fig. 9b). Superior catalytic activity of 5Ni-CeO₂^{*} catalyst was due to high surface area, better Ni dispersion, smaller Ni particle size (Table 1) and superior metal support interactions [61]. Effect of WHSV on methane conversion over 5Ni-CeO₂^{*} catalyst showed decrease in conversion after a certain value of WHSV (Supporting information Fig. S6). It was observed that the CH₄ conversion decreases to 87% when the WHSV value

was increased to 200,000 $\text{mlg}^{-1} \text{h}^{-1}$. Cerium oxide modifies the structural and electronic properties of catalysts and act as a very powerful promoter [5]. The oxygen storage and releasing properties (Redox properties) of cerium oxide is a very important feature of a support, which enhanced the carbon removal mechanism from catalyst surface during catalysis [5,61,78,79]. The H₂-TPR pattern showed metal support interaction (Fig. 2), which highly influenced the catalytic activity of catalysts. Very small size of CeO₂* nanoparticles having more lattice vacancies and increased oxygen mobility, enhanced the reducibility of nickel species, which lowered the ignition temperature (the minimum temperature at which methane will ignite without any external flame) [26]. 5Ni-CeO₂* catalyst having the smallest CeO₂ particles among 5Ni-CeO₂*, 5Ni-CeO₂^{Imp} and 5Ni-CeO₂^{Com} catalysts (Table 1), showed the superior catalytic activity [26]. Again, highly dispersed Ni species played the most important role for superior activity of 5Ni-CeO₂* catalyst, which was very low in case of 5Ni-CeO₂^{Imp} and 5Ni-CeO₂^{Com} catalysts (Table 1) [4,24,53]. Increase in nickel particle size decreased the interfacial area of Ni and CeO₂ and effectively reduced the cleaning mechanism and catalytic activity [4,24,53]. XRD pattern of 5Ni-CeO₂^{Imp} and 5Ni-CeO₂^{Com} catalysts showed formation of larger/agglomerated nickel crystals (Fig. 1A), which was also supported by SEM and TEM analysis and it was a reason for lower activity of these two catalysts [80]. Larger nickel species of 5Ni-CeO₂^{Imp} and 5Ni-CeO₂^{Com} catalysts (Table 1) were more sensitive towards coking, which suppressed the partial oxidation reaction [61]. Fig. 9b-d shows the selectivity of products and H₂/CO ratio over 5Ni-CeO₂*, 5Ni-CeO₂^{Com} and 5Ni-CeO₂^{Imp} catalysts. The obtained results showed dependence of product selectivity on Ni particle size, methane conversion and temperature. With increase in temperature, methane conversion, selectivity of CO and H₂/CO ratio increased, which was in agreement with the earlier literature reports [22,81]. Both POM and complete methane oxidation are exothermic reaction but at lower temperature, complete methane oxidation is favored over POM [21], which was also evident from the presence of CO₂ and water, with higher CO₂ selectivity over CO (Fig. 9c and d). Selectivity of CO and H₂/CO ratio was observed to be increasing with decreasing nickel particle size (Fig. 9). CO selectivity and H₂/CO ratio was superior over smaller nickel species (5Ni-CeO₂*, Fig. 9b). Same observations were reported over Rh nanoparticles by Kondratenko et al. [22]. Controlled deposition of nickel nanoparticles with smaller size led to superior activity of 5Ni-CeO₂* catalyst [5,36] over 5Ni-CeO₂^{Com} (Fig. 9c) and 5Ni-CeO₂^{Imp} (Fig. 9d) catalysts. It can be seen that the H₂/CO ratio for 5Ni-CeO₂^{Imp} and 5Ni-CeO₂^{Com} catalysts was low as compared to 5Ni-CeO₂* catalyst. The reason may be due to further oxidation of produced hydrogen by oxygen or also could be due to reverse water gas shift (RWGS) reaction ($\text{H}_2 + \text{CO}_2 \rightarrow \text{CO} + \text{H}_2\text{O}$). As there was much higher CO₂ selectivity observed for 5Ni-CeO₂^{Imp} and 5Ni-CeO₂^{Com} catalysts, the possibility of RWGS could not be excluded (at $\geq 650^\circ\text{C}$). Much larger nickel species could be responsible for the observed results for 5Ni-CeO₂^{Imp} and 5Ni-CeO₂^{Com} catalysts.

Adsorbed methane dissociated on active Ni surface and produced hydrogen and carbon species ($\text{CH}_{x=0-3}$) and these carbon species easily moved to the interface of Ni-CeO₂*, which reduced CeO₂* support adjacent to the Ni species and produced CO [78]. Very small CeO₂* nanocrystals provided very high amount of mobile oxygen, which played a significant role in methane conversion and syngas production [26]. TGA analysis showed that amount of solid carbon accumulation on catalyst surface increased with increasing nickel particle size (Fig. 8). 5Ni-CeO₂^{Imp} catalyst with larger nickel species showed maximum solid carbon accumulation on catalyst surface during catalysis (Fig. 8f). This was one reason that 5Ni-CeO₂^{Imp} and 5Ni-CeO₂^{Com} catalysts showed lower activity as the deposition of carbon with time decreased the active

sites for methane activation (Fig. 11) [42,59]. The synergy between smaller nickel species (nanoparticles, 5.5 nm) and 30–50 nm CeO₂* nanocrystals was the main driving force for better activity of 5Ni-CeO₂* catalyst [78]. The obtained results showed that the stability of Ni-CeO₂ catalysts was dependent on nickel species dispersion [43,61]. Due to insufficient surface oxygen of 5Ni-CeO₂^{Imp} and 5Ni-CeO₂^{Com} catalysts caused by larger and agglomerated catalyst particles, deposited carbon was not completely removed and with time amount of deposited carbon keep on increasing [10,25].

In Ni-CeO₂* catalysts, a synergistic effect between Ni nanoparticles and CeO₂* nanoparticles played a very active role for methane conversion [25,81]. Fig. 10 depicted the catalytic activity of different Ni-CeO₂* catalysts depending on nickel loading. We have carried out POM over Ni-CeO₂* catalyst by varying the percentage of nickel loading on the catalysts and the experimented results showed that 5 wt% Ni loading is optimum (Fig. 10c). All the Ni-CeO₂* catalysts activated methane at 400 °C. Both 2.5Ni-CeO₂* and 10Ni-CeO₂* catalyst showed complete oxidation of methane at this temperature but only 5Ni-CeO₂* catalyst showed POM activity at 400 °C. The characterization techniques revealed that 5Ni-CeO₂* have 5.5 nm nickel species (nanoparticles) supported on 30–50 nm CeO₂* nanoparticles. With increasing Ni loading, it was observed that Ni species size increased (Table 1). Nickel species dispersion of Ni-CeO₂* catalyst was noted to be decreased from 27.4% to 17.3%, when Ni loading was increased from 2.5 wt% to 10 wt%. From metal dispersion analysis it was observed that 2.5Ni-CeO₂* had Ni species of average 4.7 nm, 5Ni-CeO₂* had average Ni species size 5.5 nm and 10Ni-CeO₂* had Ni species size of 8.2 nm (Table 1). It was observed that all the catalysts were active for POM, but the activity was varied according to Ni species dispersion, Ni species size, reducibility of the Ni species and the interaction between nickel species and cerium oxide particles [4,5,24,53,60]. Fractional density of the corner and edge metal atoms increased with increasing nickel species dispersion, which facilitated the cleavage of C–H bond of CH₄ molecules on the corner and edge metals atoms [22]. Despite of higher nickel loading 10Ni-CeO₂* catalyst had lower number ($2.20 \times 10^{15}/\text{g cat.}$) of nickel species per gram catalyst compared to 2.5Ni-CeO₂* ($2.25 \times 10^{15}/\text{g cat.}$) and showed lower catalytic activity than other two Ni-CeO₂* catalysts. 2.5Ni-CeO₂* having smaller Ni species (4.7 nm) is supposed to have better metal support interaction between nickel species and CeO₂* particles but lower number of nickel species per gram catalyst limited its activity, whereas 10Ni-CeO₂* catalyst had lowest activity among these three catalysts due to its larger Ni-particle size (8.2 nm) and lowest number of nickel species per gram catalyst [22]. 5Ni-CeO₂* having well balanced particle size (5.5 nm) and number of particles per gram catalyst ($3.06 \times 10^{15}/\text{g cat.}$) showed superior results. With increasing metal dispersion, the particle size of nickel species decreased in the order 10Ni-CeO₂* > 5Ni-CeO₂* > 2.5Ni-CeO₂*, and the interfacial surface area increased. But total interfacial surface area is combined effect of metal particles size and the number of active particles. So, the total interfacial surface area of nickel and support CeO₂*, which influenced the catalytic activity of the catalyst is in the order 5Ni-CeO₂* > 2.5Ni-CeO₂* > 10Ni-CeO₂*. Fig. 10 also support the fact that CH₄ conversion over these catalysts followed the order 5Ni-CeO₂* > 2.5Ni-CeO₂* > 10Ni-CeO₂* as activity is not solely dependent on active particles size but depends on metal (Ni)-support (CeO₂*) interfacial surface area.

Strong metal support interaction between Ni species and CeO₂* nanocrystals was the main driving force for better activity of Ni-CeO₂* catalysts [4,5,24,53]. The catalytic results of Ni-CeO₂* catalysts revealed that selectivity of CO and H₂/CO ratio was dependent on number of nickel species per gram catalyst and nickel species size [22,34,82]. The catalyst (2.5Ni-CeO₂*) with smallest nickel species size (4.7 nm) showed better CO selectivity and H₂/CO ratio (Fig. 10b), whereas the catalyst (5Ni-CeO₂*) with greater

number of nickel species per gram catalyst with comparatively moderate nickel particle size (5.5 nm) showed moderate CO selectivity and H₂/CO ratio (Fig. 10c). 10Ni-CeO₂* catalyst having lowest number of nickel species per gram catalyst and larger nickel species size (8.2 nm) among these Ni-CeO₂* catalysts, showed least activity (Fig. 10d). TGA analysis (Fig. 8) also indicated that catalysts with smaller particles have much better sintering and coke resisting property with better metal support interaction, which is resistant towards particles sintering and coke deposition showed superior catalytic results. TGA results showed absolutely negligible amount of coke deposition, which was not even detected during the analysis for 2.5Ni-CeO₂* catalyst (Fig. 8b). TEM analysis also revealed that nickel particle size remained unchanged, which was the best feature of the 2.5Ni-CeO₂* catalyst (Fig. 5a). 5Ni-CeO₂* catalyst showed little bit of coking (0.6% graphitic carbon) on catalyst surface and the carbon deposition increased over 10Ni-CeO₂* catalyst (1.8% graphitic carbon) indicating that catalyst having the larger nickel species (Table 1) are not that good coke resistant and the type of solid carbon deposition was also increased with increasing nickel species size (Fig. 8). The TEM analysis also showed a hint of sintering of nickel species of 10Ni-CeO₂* catalysts (Fig. 5c). This might also be a reason for lower activity of 10Ni-CeO₂* catalyst. To optimize the nickel loading for the Ni-CeO₂* catalyst, we have to consider: (i) the CH₄ conversion, (ii) selectivity of the POM products (CO and H₂), (iii) H₂/CO ratio, (iv) minimum temperature to get syngas and (v) coke resisting ability of the catalyst. Comparing all these results for 2.5Ni-CeO₂* and 5Ni-CeO₂* catalysts, it can be seen that CH₄ conversion was always higher for 5Ni-CeO₂* catalyst (Fig. 10a), selectivity of CO, H₂ and H₂/CO ratio was little lower at lower temperature but comparable at temperature range between 650 and 800 °C (Fig. 10b, 10c), minimum temperature to get syngas (i.e. POM) was 400 °C for 5Ni-CeO₂* catalyst but it was 450 °C for 2.5Ni-CeO₂* catalyst (Fig. 10b and c) and the coke resisting ability of the 2.5Ni-CeO₂* catalyst was just little higher because the nickel species size was smaller than 5Ni-CeO₂* catalyst (Fig. 8b and c). So, considering all these, we observed that 5Ni-CeO₂* catalyst was superior and 5 wt% nickel loading was optimum.

The stability of different catalysts was tested at 800 °C. Fig. 11a–e shows the time on stream stability of 2.5Ni-CeO₂*, 5Ni-CeO₂*, 10Ni-CeO₂*, 5Ni-CeO₂^{Imp} and 5Ni-CeO₂^{Com} catalysts. 5Ni-CeO₂* catalyst showed 90 h of TOS stability (Fig. 11f) and after that a small decrease in activity was observed because of small amount of coke deposited on catalyst surface (Fig. 8c). About 100 h of TOS stability of 5Ni-CeO₂* catalyst indicated that the particle size remains unchanged during the catalysis [22]. 5Ni-CeO₂* catalyst TEM image after 100 h TOS supported the fact that the nickel species size remained almost unchanged (Supporting information Fig. S7). 5Ni-CeO₂^{Com} catalyst (Fig. 11d) showed very slow decrease in activity during first 7 h then rapid decrease in activity was observed. The decrease in activity of 5Ni-CeO₂^{Com} catalyst was caused by the sintering and coke deposition on catalyst surface, which was also supported by XRD (Fig. 1Bd), SEM (Fig. 3f), TEM (Figs. 5e and 6b) and TGA (Fig. 8e) analysis. 5Ni-CeO₂^{Imp} catalyst (Fig. 11e) showed continuous decrease in activity from the beginning of TOS experiment, which indicated the change in catalysts physical properties during catalysis (Table 1) [22]. The characterization techniques also revealed the changes in physical properties of 5Ni-CeO₂^{Imp} catalyst (Figs. 1Be, 3e, 5d and 8f). 5Ni-CeO₂^{Imp} catalyst showed maximum amount of solid coke deposition after catalysis (Fig. 8f) due to very low metal support interaction because of larger nickel species formed during impregnation. Although the 5Ni-CeO₂^{Imp} catalyst was synthesized by impregnating nickel on smaller and uniformly shaped CeO₂* particles, yet the 5Ni-CeO₂^{Imp} catalyst showed continuous decrease in activity (Fig. 11e) due to very low metal support interaction, which led to catalyst sintering and coke deposition right from the beginning of TOS experiment [8]. Therefore, the catalyst syn-

thesis procedure played the crucial role for 5Ni-CeO₂^{Imp} catalysts deactivation. 5Ni-CeO₂* catalyst with smaller Ni species showed superior TOS stability (Fig. 11f) due to its better metal support interaction between nickel species and CeO₂* nanocrystals, whereas the 5Ni-CeO₂^{Com} catalyst having larger nickel species with very low metal support interaction between nickel species and non-uniform size and shaped larger CeO₂^{Com} crystals was unable to show much higher activity (Fig. 11d) [34,82,83]. The first 7 h of stability of 5Ni-CeO₂^{Com} catalyst was may be due to metal support interaction generated as an effect of the nickel deposition procedure [5]. TGA analysis showed huge amount of coke deposition as graphitic carbon and/or carbon nanotubes on 5Ni-CeO₂^{Imp} and 5Ni-CeO₂^{Com} with 4.7 wt% and 3.9 wt% respectively, whereas for the 5Ni-CeO₂* catalyst the amount (0.6 wt%) was very low (Table 3, Fig. 8). Different nickel particle sizes with different metal support interaction caused the generation of different kinds of carbon. Although, spent 10Ni-CeO₂* showed a good amount (4.6 wt%) of hydrogen containing carbon species (CH_x) (Fig. 8d) but it did not affect the activity of the catalysts that much (Fig. 11c) [84]. TGA analysis (Fig. 8) and the TOS study (Fig. 11) confirmed that the type of deposited carbon is dependent on nickel particle size and hydrogen containing carbon species (CH_x) is not the reason for catalysts deactivation, it is the graphitic carbon and/or carbon nanotubes are responsible for catalysts deactivation. A comparative analysis with the literature reports also showed superiority of Ni-CeO₂* catalyst and the controlled deposition method for catalyst preparation (Supporting information, Table S1)

4.2. Kinetic analysis

POM is an exothermic reaction and the catalyst bed temperature can be increased by the heat released during catalysis. The kinetic analysis was carried out at the reaction condition at which the diffusion limitations can be neglected. Conversion of methane was checked by varying WHSV and pellet size, catalyst weight, keeping the same methane flow rate to bed length ratio, methane feed rate, W/F (weight/flow) and observed that the change in methane conversion was negligible (Supporting information Figs. S8 and S9). Under mass transfer limitation, increase in catalyst amount hinders the accessibility of active sites as it inhibits the diffusion of reactant molecules inside the catalyst pores, as reported by Balint et al. [46]. We have carried out this test and found that the increase in catalyst amount did not affect methane conversion (Supporting information Fig. S8b) and the observation led us to rule out the transport limitations [5,34]. We also carried out the mathematical calculations for Heat and Mass transfer limitations as described by Oyama et al. (Supporting information) [85].

The Weisz-Prater Criterion

$$C_{WP} = \frac{-r'_A(\text{obs})\rho_c R^2}{D_e C_{As}} = 0.1476 < 1$$

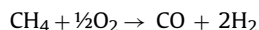
The Mears Criterion

$$\frac{-r'_A \rho_b R n}{k_c C_{Ab}} = 0.0582 < 0.15$$

The Weisz-Prater Criterion and the Mears Criterion calculation indicated that there was no internal and external diffusion over 5Ni-CeO₂* catalyst during catalysis.

The kinetic response of methane conversion rates to CH₄ and O₂ pressures was measured on 5Ni-CeO₂* catalyst in a fixed bed reactor by varying inlet concentrations. Without a catalyst, no reaction products were observed. Measured CH₄ conversion rates ($-r_{\text{CH}_4}$) were proportional to $P_{\text{CH}_4}P_{\text{O}_2}^{1/2}$, where P_{CH_4} is the partial pressure of methane and $P_{\text{O}_2}^{1/2}$ is the partial pressure of oxygen. The rate

of reaction in respect to methane consumption was studied using 5Ni-CeO₂* catalyst.



Reaction rate is also a function of partial pressures of different reactants of the reaction. For POM, the power rate law expression can be written as follows.

$$-\dot{r}_{\text{CH}_4} = k \cdot (\text{P}_{\text{CH}_4})^B \cdot (\text{P}_{\text{O}_2})^C$$

Where, k, B and C are the unknown parameters to be determined.

k = rate constant, B = reaction order in respect to methane and C = reaction order in respect to oxygen.

The kinetic experiments were carried out at methane conversion less than 10% in the temperature range 375–395 °C. The parameters were calculated by Polymath 5.1 software. Previous reports suggested that the oxygen atom located at the top site of metal increases the adsorption energy of H (hydrogen) and promotes methane dissociation [86]. It is also reported that production of CO and CO₂ are slower than C–H bond cleavage of methane [68] and the overall reaction order for catalytic POM is ≤ 1 [87]. In our study, we also observed that the overall reaction order is less than 1 and the reaction rate depends on partial pressures of both reactants. Reaction rates with the change in partial pressure of methane and O₂ are represented in Fig. 12. The kinetic parameters are given in Table 6. The Arrhenius model was applied for the estimation of activation energy for methane (Fig. 12c) in POM over 5Ni-CeO₂* catalyst. The activation energy for methane was calculated to be 72.70 kJ/mol and the observation is in agreement with the earlier reports [5].

5. Conclusion

The Ni-CeO₂* catalyst was synthesized by two step method. The method of nickel deposition over the support CeO₂ played most important role for the formation of different sized nickel species and metal support interaction between nickel species and nanoparticles of CeO₂. During controlled deposition of nickel, cetyltrimethylammonium bromide (CTAB) played the role of morphology controlling agent for nickel species and polyvinylpyrrolidone acted as particle size controlling agent. 5 wt% Ni loading was the optimum value for catalytic activity of Ni-CeO₂* catalyst with superior conversion and product selectivity. The synergy between smaller nickel species (~ 5 nm) and CeO₂* nanocrystals with size 30–50 nm was the main driving force for 5Ni-CeO₂* catalysts activity, which actives methane at 400 °C for POM and the catalyst remained stable for 90 h without any significant activity loss at 800 °C. During time on stream reaction, the catalyst maintained H₂/CO ratio at 1.98 throughout the 90 h time, which was the main advantage of 5Ni-CeO₂* catalyst. The stability of Ni-CeO₂ catalysts depends on nickel dispersion. Nickel particle size and metal support interaction controlled the type of deposited carbon on catalyst surface during catalysis. Smaller nickel species with better metal support interaction were most resistant toward coking. The study also revealed that it is not only the amount but the type of carbon (graphitic carbon and/or carbon nanotubes) is the most affecting reason for catalysts deactivation. Graphitic carbon and/or carbon nanotubes were observed to be deposited mainly over the catalysts consisting larger nickel crystals during POM reaction.

Acknowledgments

R.S. thanks UGC, New Delhi, India for their fellowships. R.B. thanks CSIR for funding in the form of Network Project (CSC-0125, CSC-0117), DST Government of India for funding in the

form of AISRF Grand Challenge Project (DST/INT/Aus/GCP-4/13(C)), Nanomission Scheme (SR/NM/NS-1105/2015). The Director, CSIR-IIP, is acknowledged for his help and encouragement. The authors thank the Analytical Science Division, Indian Institute of Petroleum for analytical services.

Appendix A. Supplementary data

Supplementary data associated with this article can be found, in the online version, at <http://dx.doi.org/10.1016/j.apcatb.2016.09.060>.

References

- [1] T.V. Choudhary, V.R. Choudhary, *Angew. Chem. Int. Ed.* 47 (2008) 1828–1847.
- [2] S.S. Bharadwaj, L.D. Schmidt, *Fuel Process. Technol.* 42 (1995) 109–127.
- [3] R.K. Singha, A. Shukla, S. Adak, C. Pendem, S. Saran, R. Bal, *Indian J. Chem.* 53A (2014) 467–471.
- [4] R.K. Singha, A. Yadav, A. Agrawal, A. Shukla, S. Adak, T. Sasaki, R. Bal, *Appl. Catal. B: Environ.* 191 (2016) 165–178.
- [5] R.K. Singha, S. Ghosh, S.S. Acharyya, A. Yadav, A. Shukla, T. Sasaki, A.M. Venezia, C. Pendem, R. Bal, *Catal. Sci. Technol.* 6 (2016) 4601–4615.
- [6] A.P.E. York, T. Xiao, M.L.H. Green, *Top. Catal.* 22 (2003) 345–358.
- [7] J.R.R. Nielsen, *Catal. Today* 18 (1993) 305–324.
- [8] S. Zhang, S. Muratsugu, N. Ishiguro, M. Tada, *ACS Catal.* 3 (2013) 1855–1864.
- [9] S. Boullous-Eiras, T. Zhao, E. Vanhaecke, D. Chen, A. Holmen, *Catal. Today* 178 (2011) 12–24.
- [10] Y.J.O. Asencios, P.A.P. Nascente, E.M. Assaf, *Fuel* 97 (2012) 630–637.
- [11] A.J. Majewski, J. Wood, *Int. J. Hydrogen Energy* 39 (2014) 12578–12585.
- [12] H. Tanaka, R. Kaino, K. Okumura, T. Kizuka, K. Tomishige, *J. Catal.* 268 (2009) 1–8.
- [13] C.T. Au, H.Y. Wang, H.L. Wan, *J. Catal.* 158 (1996) 343–348.
- [14] Y.H. Hu, E. Ruckenstein, *J. Catal.* 158 (1996) 260–266.
- [15] L. Li, S. He, Y. Song, J. Zhao, W. Ji, C.T. Au, *J. Catal.* 288 (2012) 54–64.
- [16] C. Berger-Karin, J. Radnik, E.V. Kondratenko, *J. Catal.* 280 (2011) 116–124.
- [17] B. Irigoyen, N. Castellani, A. Juan, *J. Mol. Catal. A* 129 (1998) 297–310.
- [18] H.C. Yao, Y.F.Y. Yao, *J. Catal.* 86 (1984) 254–265.
- [19] W. Liu, M.F. Stephanopoulos, *Chem. Eng. J.* 64 (1996) 283–294.
- [20] A. Trovarelli, C. de Leitenburg, G. Dolcetti, *Chemtech* 27 (1997) 32–40.
- [21] A. Scarabello, D.D. Nogare, P. Canu, R. Lanza, *Appl. Catal. B: Environ.* 174 (2015) 308–322.
- [22] V.A. Kondratenko, C.B. Karin, E.V. Kondratenko, *ACS Catal.* 4 (2014) 3136–3144.
- [23] J. Ren, X. Qin, J.Z. Yang, Z.F. Qin, H.L. Guo, J.Y. Lin, Z. Li, *Fuel Process. Technol.* 137 (2015) 204–211.
- [24] R.K. Singha, A. Shukla, A. Yadav, S. Adak, Z. Iqbal, N. Siddiqui, R. Bal, *Appl. Energy* 178 (2016) 110–125.
- [25] A.I. Paksoy, B.S. Caglayan, A.E. Aksoylu, *Appl. Catal. B: Environ.* 168 (2015) 164–174.
- [26] S.B. Eiras, T. Zhao, D. Chen, A. Holmen, *Catal. Today* 171 (2011) 104–115.
- [27] V.A. Kirillov, Z.A. Fedorova, M.M. Danilova, V.I. Zaikovskii, N.A. Kuzin, V.A. Kuzmin, T.A. Krieger, V.D. Mescheryakov, *Appl. Catal. A: Gen.* 401 (2011) 170–175.
- [28] L. Li, Y. Yao, B. Sun, Z. Fei, H. Xia, J. Zhao, W. Ji, Chak-Tong Au, *ChemCatChem* 5 (2013) 3781–3787.
- [29] A.S. Larimi, S.M. Alavi, *Int. J. Chem. Eng. Appl.* 3 (2012) 6–9.
- [30] H. Oezdemir, O.M.A. Faruk, G.M. Ali, *Fuel* 116 (2014) 63–70.
- [31] G. Pantaleo, V.L. Parola, F. Deganello, P. Calatozzo, R. Bal, A.M. Venezia, *Appl. Catal. B: Environ.* 164 (2015) 135–143.
- [32] G. Pantaleo, V. La Parola, F. Deganello, R.K. Singha, R. Bal, A.M. Venezia, *Appl. Catal. B: Environ.* 189 (2016) 233–241.
- [33] R.L. Oliveira, I.G. Bitencourt, F.B. Passos, J. Braz. Chem. Soc. 24 (2013) 68–75.
- [34] J. Wei, E. Iglesia, *J. Catal.* 224 (2004) 370–383.
- [35] Z.Y. Hou, O. Yokota, T. Tanaka, T. Yashima, *Catal. Lett.* 89 (1–2) (2003) 121–127.
- [36] J.L. Ewbank, L. Kovarik, C.C. Kenvina, C. Sievers, *Green Chem.* 16 (2014) 885–896.
- [37] D. Baudouin, U. Rodemerck, F. Krumeich, A. de Mallmann, K.C. Szeto, H. Ménard, L. Veyre, J.P. Candy, P.B. Webb, C. Thieuleux, C. Copéret, *J. Catal.* 297 (2013) 27–34.
- [38] A. Djaidja, S. Libs, A. Kienemann, A. Barama, *Catal. Today* 113 (2006) 194–200.
- [39] M. Fleys, Y. Simon, D. Swierczynski, A. Kienemann, P.M. Marquaire, *Energy Fuels* 20 (2006), 2321–2319.
- [40] L. Pino, A. Vita, F. Cipiti, M. Laganà, V. Recupero, *Appl. Catal. B: Environ.* 104 (2011) 64–73.
- [41] R. Zanganeh, M. Rezaei, A. Zamaniyan, *Int. J. Hydrogen Energy* 38 (2013) 3012–3018.
- [42] Y. Song, H. Liu, S. Liu, D. He, *Energy Fuels* 23 (2009) 1925–1930.
- [43] T. Zhu, M.F. Stephanopoulos, *Appl. Catal. A: Gen.* 208 (2001) 403–417.
- [44] G. Delahay, D. Valade, A.G. Vargas, B. Coq, *Appl. Catal. B: Environ.* 55 (2005) 149–155.

- [45] B.M. Abu-Zied, W. Schwieger, A. Unger, *Appl. Catal. B: Environ.* 84 (2008) 277–288.
- [46] I. Balint, A. Miyazaki, K. Aika, *J. Catal.* 220 (2003) 74–83.
- [47] G.C. Bond, Platin. Metals Rev. 19 (1975) 126–134.
- [48] X. Du, D. Zhang, L. Shi, R. Gao, J. Zhang, *J. Phys. Chem. C* 116 (2012) 10009–10016.
- [49] V.M. Gonzalez-dela Cruz, J.P. Holgado, R. Pereñiguez, A. Caballero, *J. Catal.* 257 (2008) 307–314.
- [50] A. Caballero, J.P. Holgado, V.M. Gonzalez-dela Cruz, S.E. Habas, T. Herranz, M. Salmeron, *Chem. Commun.* 46 (2010) 1097–1099.
- [51] H. Zhu, Z. Qin, W. Shan, W. Shen, J. Wang, *J. Catal.* 225 (2004) 267–277.
- [52] X. Zhang, Q. Zhang, N. Tsubaki, Y. Tan, Y. Han, *Fuel* 147 (2015) 243–252.
- [53] R.K. Singha, A. Yadav, A. Shukla, Z. Iqbal, C. Pendem, K. Sivakumar, R. Bal, *ChemistrySelect* 1 (2016) 3075–3085.
- [54] L. Pino, A. Vita, M. Córdaro, V. Recupero, M.S. Hegde, *Appl. Catal. A: Gen.* 243 (2003) 135–146.
- [55] W.P. Dow, Y.P. Wang, T.J. Huang, *J. Catal.* 160 (1996) 155–170.
- [56] M. Zabilskiy, P. Djinović, E. Tchernykhova, O.P. Tkachenko, L.M. Kustov, A. Pintar, *ACS Catal.* 5 (2015) 5357–5365.
- [57] S.S. Acharyya, S. Ghosh, S. Adak, R. Singh, S. Saran, R. Bal, J. Nanosci. Nanotechnol. 15 (2015) 1–7.
- [58] Z. Li, L. Mo, Y. Kathiraser, S. Kawi, *ACS Catal.* 4 (2014) 1526–1536.
- [59] H. Jiang, H. Li, H. Xu, Y. Zhang, *Fuel Process. Technol.* 88 (2007) 988–995.
- [60] R.K. Singha, S. Das, M. Pandey, S. Kumar, R. Bal, A. Bordoloi, *Catal. Sci. Technol.* (2016), <http://dx.doi.org/10.1039/c5cy01323b>.
- [61] A. Shamsi, *Appl. Catal. A: Gen.* 277 (2004) 23–30.
- [62] K. Nagaoka, M. Okamura, K. Aika, *Catal. Commun.* 2 (2001) 255–260.
- [63] K. Tomishige, Y.G. Chen, K. Kujimoto, *J. Catal.* 181 (1999) 91–103.
- [64] J.H. Bitter, K. Seshan, J.A. Lercher, *J. Catal.* 183 (1999) 336–343.
- [65] J.B. Branco, A.C. Ferreira, T.A. Gasche, G. Pimenta, J.P. Leal, *Adv. Synth. Catal.* 356 (2014) 3048–3058.
- [66] D.A. Hickman, L.D. Schmidt, *Science* 259 (1993) 343–346.
- [67] E.P.J. Mallens, J.H.B.J. Hoebink, G.B. Marin, *J. Catal.* 167 (1997) 43–56.
- [68] Y.H. Hu, E. Ruckenstein, *J. Phys. Chem. A* 102 (1998) 10568–10571.
- [69] D. Dissanayake, M.P. Rosynek, K.C.C. Kharas, J.H. Lunsford, *J. Catal.* 132 (1991) 117–127.
- [70] R.A. Campbell, J.P. Lenz, D.W. Goodman, *Catal. Lett.* 17 (1993) 39–46.
- [71] Q.G. Yan, T.H. Wu, W.Z. Weng, H. Toghiani, R.K. Toghiani, H.L. Wan, C.U. Pittman, *J. Catal.* 226 (2004) 247–259.
- [72] I. Tavazzi, A. Beretta, G. Groppi, P. Forzatti, *Stud. Surf. Sci. Catal.* 147 (2004) 163–168.
- [73] F.V. Looij, J.W. Geus, *J. Catal.* 168 (1997) 154–163.
- [74] C.T. Au, H.Y. Wang, *Catal. Lett.* 41 (1996) 159–163.
- [75] E. Ruckenstein, Y.H. Hu, *Appl. Catal. A: Gen.* 183 (1999) 85–92.
- [76] S. Rabe, T.B. Truong, F. Vogel, *Appl. Catal. A: Gen.* 292 (2005) 177–188.
- [77] T. Wu, Q. Yan, H. Wan, *J. Mol. Catal. A* 226 (2005) 41–48.
- [78] A. Luengnaruemitchai, S. Osuwan, E. Gulari, *Catal. Commun.* 4 (2003) 215–222.
- [79] H.S. Roh, K.W. Jun, W.S. Dong, S.E. Park, Y.S. Baek, *Catal. Lett.* 74 (2001) 31–36.
- [80] B.Q. Xu, J.M. Wei, Y.T. Yu, Y. Li, J.L. Li, Q.M. Zhu, *J. Phys. Chem. B* 107 (2003) 5203–5207.
- [81] J.M. García-Vargas, J.L. Valverde, A. de Lucas-Consuegra, B. Gómez-Monedero, P. Sánchez, F. Dorado, *Appl. Catal. A: Gen.* 431–432 (2012) 49–56.
- [82] L.B. Råberg, M.B. Jensen, U. Olsbye, C. Daniel, S. Haag, C. Mirodatos, A. Olafsen Sjåstad, *J. Catal.* 249 (2007) 250–260.
- [83] D.A.J.M. Ligthart, R.A. van Santen, E.J.M. Hensen, *J. Catal.* 280 (2011) 206–220.
- [84] M. García-Díéguez, I.S. Pieta, M.C. Herrera, M.A. Larrubia, L.J. Alemany, *J. Catal.* 270 (2010) 136–145.
- [85] S.T. Oyama, X. Zhang, J. Lu, Y. Gu, T. Fujitani, *J. Catal.* 257 (2008) 1–4.
- [86] C.T. Au, M.S. Liao, C.F. Ng, *J. Phys. Chem. A* 102 (1998) 3959–3969.
- [87] A. Donazzi, A. Beretta, G. Groppi, P. Forzatti, *J. Catal.* 255 (2008) 241–258.